

# A p-adaptive, implicit-explicit mixed finite element method for reaction-diffusion problems

Mebratu Wakeni<sup>a</sup>, Ankush Aggarwal<sup>a</sup>, Lukasz Kaczmarczyk<sup>a</sup>, Andrew McBride<sup>a</sup>, Ignatios Athanasiadis<sup>a</sup>, Chris Pearce<sup>a</sup>, Paul Steinmann<sup>a,b</sup>

<sup>a</sup>*Glasgow Computational Engineering Centre, University of Glasgow, Glasgow, G12 8QQ, United Kingdom*

<sup>b</sup>*Institute of Applied Mechanics, Friedrich-Alexander University of Erlangen-Nuremberg, Paul-Gordan-Str. 3, D-91052, Erlangen, Germany*

---

## Abstract

A new class of implicit-explicit (IMEX) methods combined with a p-adaptive mixed finite element formulation is proposed to simulate the diffusion of reacting species. Hierarchical polynomial functions are used to construct an  $H(\text{div})$ -conforming base for the flux vectors, and a non-conforming  $L^2$  base for the mass concentration of the species. The mixed formulation captures the distinct nonlinearities associated with the constitutive flux equations and the reaction terms. The IMEX method conveniently treats these two sources of nonlinearity implicitly and explicitly, respectively, within a single time-stepping framework. The combination of the p-adaptive mixed formulation and the IMEX method delivers a robust and efficient algorithm. The proposed methods eliminate the coupled effect of mesh size and time step on the algorithmic stability. A residual based a posteriori error estimate that provides an upper bound of the natural error norm is derived. The availability of such estimate which can be obtained with minimal computational effort and the hierarchical construction of the finite element spaces allow for the formulation of an efficient p-adaptive algorithm. A series of numerical examples demonstrate the performance of the approach. It is shown that the method with the p-adaptive strategy accurately solves problems involving travelling waves, and those with discontinuities and singularities. The flexibility of the formulation is also illustrated via selected applications in pattern formation and electrophysiology.

**Keywords:** Implicit-explicit method; Mixed formulation; Hierarchical basis functions;  $H(\text{div})$ -conforming; Reaction-diffusion equation; p-adaptivity

---

## 1. Introduction

### 1.1. Motivation

The spatio-temporal dynamics of multiple species interacting through a combination of two distinct mechanisms, namely reaction and diffusion, can be described by *reaction-diffusion* equations. Reaction refers to the inter/intra species interactions, resulting in the production and extinction of species. It is embodied in a term that is referred to as *reaction kinetics*  $f$ , a function of the mass concentration(s)  $m$  of the involved species. Diffusion refers to the flow of substance (concentration) in space, and it is mathematically described by a flux  $\mathbf{h}$  related to  $m$  (and/or its spatial gradient) through a constitutive equation. Reaction-diffusion models are relevant in various important applications, including tissue morphogenesis and pattern formation [1–4], tissue remodelling [5–10], electrophysiology [11, 12], and epidemiology [13–15].

The aforementioned applications motivate the need for robust and efficient numerical methods for solving reaction-diffusion problems. Various numerical methods have been proposed for approximating the solutions of reaction-diffusion problems. Meshless methods in conjunction with operator-splitting techniques were used in [16] in one- and two-dimensions. In [17], Fitzhugh-Nagumo type models are solved using a multidomain algorithm based on a pseudospectral approach. A review of some finite difference based methods in one-dimension can be found in [18]. Furthermore, a finite difference scheme was constructed for the simulation of waves in excitable media using a two-variable reaction-diffusion equation in [19]. However, finite difference and spectral algorithms are suitable only for approximations over relatively simple domains.

### 1.2. Spatial discretisation

The finite element method, due to its capabilities in handling arbitrary geometry and nonlinearities and its strong theoretical foundation, is a natural choice for solving reaction-diffusion problems. The majority of the finite element numerical approaches used in the literature are based on the standard, single-field formulation. The standard formulation for reaction-diffusion was employed in a computational framework for the coupling of reaction-diffusion and elasticity in [20]. In [21], a multilevel finite element approach with spatial and temporal adaptivity was constructed for reaction-diffusion problems. In [22], a projected finite element approach on stationary closed surface geometries, together with a backward Euler time integration, was used to simulate pattern-formation in biological applications. In [23], a moving mesh finite element method was constructed for simulating chemotaxis in two-dimensions. A multi-grid finite element method on stationary and evolving surfaces was proposed in [24]. A semi-linear multistep finite element was constructed in [25] for the two-dimensional simulation of pattern formation in ecological application. In such standard formulations, only the mass concentration  $m$  is solved for. The other physically important quantity, the flux  $\mathbf{h}$ , is obtained as a post-processing step, decreasing the accuracy of its approximation.

Solutions of reaction-diffusion problems exhibit a variety of phenomena from the formation of travelling waves to complex structures like dissipative solitons. Some solutions may even involve low regularity features such as evolving jump discontinuities and singularities. The  $H^1$ -conforming basis functions used in the standard formulation impose an unnecessarily high regularity requirement; for solutions displaying low regularity features the approximate solution may never converge to the true solution. Mixed finite element methods [see e.g. 26–28] offer an elegant solution for such problems. Mixed finite element methods are two-field formulations, which employ an  $H(\text{div})$ -conforming basis for the flux and a  $L^2$ -conforming basis for the mass concentration. This combination of basis functions relaxes the conformity requirements, allowing a wider class of solutions to be approximated accurately.

Numerical studies of reaction-diffusion type problems using mixed methods are, by comparison with standard formulations, relatively few. In [29], a stabilised mixed formulation in combination with a first-order implicit time integration was proposed for solving steady and unsteady state reaction-diffusion problems. In this approach,  $H^1$ -conforming finite element spaces are used for  $m$ , and  $L^2$ -conforming spaces for  $\mathbf{h}$ . With regard to the finite element space used for  $m$ , such a method has no particular advantage over the standard finite element method in terms of accuracy. A two-grid approach based on a variation of a mixed method with an implicit temporal integration was proposed and analysed in [30].

### 1.3. Temporal discretisation

Most numerical procedures for reaction-diffusion equations that utilise finite elements, usually approach the temporal integration using either fully-implicit or fully-explicit methods. It is well-established that explicit methods can be very efficient and are easy to implement, however, they usually suffer in terms of algorithmic stability, and impose severe time step restriction arising from the diffusion term [31]. Implicit methods are known for their greater stability, but can be challenging in terms of implementation, and are usually less efficient as they lead to the solution of a large system of algebraic equation. In addition, for nonlinear problems, it is necessary to derive and compute tangent matrices that includes implicit nonlinearities at each time step, adding further inefficiencies. Implicit-explicit (IMEX) methods mitigate such problems by combining the advantages of explicit and implicit methods [32]. By treating the non-local diffusion term (involving a spatial derivative) implicitly, and the local reaction term (without a spatial derivative) explicitly, one can eliminate the coupling effect of spatial mesh size  $h$  and the time step size  $\Delta t$  on the stability condition. This allows the spatial mesh to be refined adaptively without the need for reducing the time-step size. The application of IMEX methods appears conducive for reaction-diffusion problems, however, most of the literature on IMEX methods for such problems are limited to classical spatial discretisation techniques, such as finite-difference [31, 33, 34] and standard finite element [25, 35, 36].

The mixed method allows for the nonlinearities that may appear in the flux constitutive equation and the reaction term to be considered separately. For stability reasons, the flux constitutive equation must be treated implicitly, while the nonlinearities in the reaction term can be handled explicitly. In this presentation we present a robust and efficient numerical algorithm based on mixed formulation with IMEX temporal integration methods for problems of reaction-diffusion type.

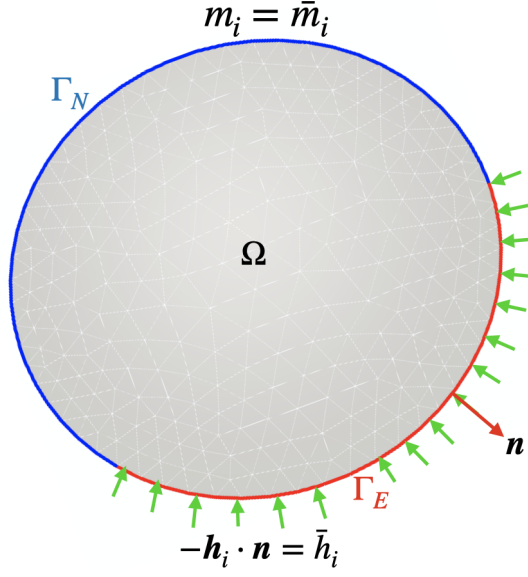


Figure 1: Schematics of the domain  $\Omega$  with its boundary partitions  $\Gamma_E$  and  $\Gamma_N$

#### 1.4. Manuscript organisation

The contribution is organised as follows. In Section 2, a general mathematical model of multi-species reaction-diffusion systems is presented briefly. The weak formulation of the model using a mixed approach, is described in Section 3. In Section 4, relevant aspects of the numerical procedure for the temporal discretisation using the IMEX method and the spatial approximation using mixed Galerkin approaches are presented. Finally, in Section 7 the performance and capabilities of the proposed formulations are demonstrated using various numerical examples. Here, the performance of the mixed and the standard formulations are compared, and finally some selected examples relevant to pattern formation, ecology, and electrophysiology are simulated using the mixed method.

## 2. Model overview

Consider  $n$  species, each with mass concentration  $m_i$ , where  $i = 1, 2, 3, \dots, n$ , interacting in an open, bounded region  $\Omega \subset \mathbb{R}^d$  ( $d = 1, 2$ , or  $3$ ). The local form of the mass balance, for each of the species, is given by

$$\dot{m}_i + \operatorname{div} \mathbf{h}_i = f_i(m_1, \dots, m_n), \quad i = 1, \dots, n, \quad (1)$$

where  $\mathbf{h}_i$  denotes the concentration flux of the  $i^{\text{th}}$  species, and  $f_i$  is the chemical kinetics term that represents the rate of production or degradation of species concentration of the  $i^{\text{th}}$  species as a result of its interaction with other species. In addition to the mass balance equation (1), a constitutive relation relating the flux  $\mathbf{h}_i$  to the mass concentration  $m_i$  is required. A commonly used constitutive relation is given by

$$\mathbf{h}_i = -\mathbf{D}_i \nabla m_i, \quad i = 1, \dots, n. \quad (2)$$

Here  $\mathbf{D}_i$  is a symmetric and positive-definite second-order tensor representing a potentially spatially varying diffusivity/mobility of the  $i^{\text{th}}$  species on the domain  $\Omega$ . Let  $\Gamma_N$  and  $\Gamma_E$  be nonoverlapping portions of the boundary of  $\Omega$ , denoted by  $\Gamma$  (see Fig. 1), such that  $\overline{\Gamma_N \cup \Gamma_E} = \Gamma$ . The prescribed boundary conditions imposed on these partitions are

$$m_i = \bar{m}_i \quad \text{on } \Gamma_N, \quad \text{and} \quad (3)$$

$$-\mathbf{h}_i \cdot \mathbf{n} = \bar{h}_i \quad \text{on } \Gamma_E, \quad (4)$$

where  $\mathbf{n}$  represents the unit outward normal vector to the boundary  $\Gamma$ . A complete description of the problem also requires the prescription of initial conditions for each  $m_i$ , which read as

$$m_i(\mathbf{x}) = m_i^0(\mathbf{x}), \quad \text{at } t = 0, \quad \forall \mathbf{x} \in \Omega.$$

### 3. Weak formulations

The focus here is on the mixed formulation. However, for the sake of completeness, the standard, single-field formulation is first briefly stated. Thereafter, a detailed presentation of the mixed formulation and its spatial and temporal discretisation is given.

In the context of initial-boundary value problems, such as analysed here, it is helpful to view functions of space and time as mappings from the time interval of interest  $\mathbb{I} = [0, T]$  to the corresponding functional space. For example, a function  $u \in L^2(\Omega; \mathbb{I})$  is understood as the map  $u : \mathbb{I} \rightarrow L^2(\Omega)$  (the space  $L^2(\Omega)$  denotes the space of measurable functions which are square integrable over the domain  $\Omega$ ). In addition to the functional space  $L^2(\Omega; \mathbb{I})$  we also make use of the space  $H^1(\Omega; \mathbb{I})$  and  $H(\text{div}, \Omega; \mathbb{I})$ , where

$$\begin{aligned} H^1(\Omega) &= \{m \in L^2(\Omega) : \nabla m \in [L^2(\Omega)]^d\}, \quad \text{and} \\ H(\text{div}, \Omega) &= \{\mathbf{h} \in [L^2(\Omega)]^d : \text{div } \mathbf{h} \in L^2(\Omega)\}. \end{aligned}$$

The natural norms endowed by  $H^1(\Omega)$  and  $H(\text{div}, \Omega)$  are, respectively, given by

$$\begin{aligned} \|m\|_{1,\Omega}^2 &:= \|m\|_{0,\Omega}^2 + \|\nabla m\|_{0,\Omega}^2, \quad \text{and} \\ \|\mathbf{h}\|_{\text{div},\Omega}^2 &:= \|\mathbf{h}\|_{0,\Omega}^2 + \|\text{div } \mathbf{h}\|_{0,\Omega}^2, \end{aligned}$$

where  $\|\cdot\|_{0,\Omega}$  denotes the standard  $L^2$ -norm for scalar or vector-valued functions.

The standard weak problem is defined as:

#### Standard formulation

find  $m_i \in H^1(\Omega)$ , satisfying the boundary conditions (3), such that

$$\frac{d}{dt}(v, m_i)_\Omega + (\nabla v, \mathbf{D}_i \nabla m_i)_\Omega = (v, \bar{h}_i)_{\Gamma_E} + \ell_i(v), \quad \forall v \in H_{0N}^1(\Omega), \quad (5)$$

where  $H_{0N}^1(\Omega)$  is a subspace of  $H^1(\Omega)$  that contains functions whose trace on  $\Gamma_N$  vanish. Here, it should be noted that the test function  $v$  is time-independent. The functional  $\ell_i : H^1(\Omega) \rightarrow \mathbb{R}$  is defined by

$$\ell_i(v) := (f_i, v)_\Omega. \quad (6)$$

The pairings  $(\cdot, \cdot)_\Omega$  and  $(\cdot, \cdot)_{\Gamma_{N/E}}$  represent the standard  $L^2$  inner product over the domain  $\Omega$  and the boundary  $\Gamma_N$  or  $\Gamma_E$ , respectively.

As can be seen from equation (5), the boundary condition (4) is incorporated into the weak form, while equation (3) is enforced as a constraint on the trial solutions. Thus, for the standard formulation, (4) is a natural boundary condition and (3) is an essential boundary condition.

For a mixed finite element formulation, in addition to  $m_i$  the flux  $\mathbf{h}_i$  is an unknown variable. Thus, the constitutive relation (2) is re-written as

$$\mathbf{D}_i^{-1} \mathbf{h}_i + \nabla m_i = \mathbf{0}. \quad (7)$$

The mixed weak form associated with equations (7) and (1) reads:

### Mixed formulation

find  $(\mathbf{h}_i, m_i) \in H_E(\text{div}, \Omega; \mathbb{I}) \times L^2(\Omega; \mathbb{I})$  such that

$$a_i(\boldsymbol{\tau}, \mathbf{h}_i) - b(\boldsymbol{\tau}, m_i) = (\boldsymbol{\tau} \cdot \mathbf{n}, \bar{m}_i)_{\Gamma_N}, \quad \forall \boldsymbol{\tau} \in H_{0E}(\text{div}, \Omega) \quad (8)$$

$$\frac{d}{dt} c(v, m_i) + b(\mathbf{h}, v) = \ell_i(v), \quad \forall v \in L^2(\Omega) \quad (9)$$

where the spaces  $H_E(\text{div}, \Omega)$  and  $H_{0E}(\text{div}, \Omega)$  are subspaces of  $H(\text{div}, \Omega)$ . Also, the test functions  $v$  and  $\boldsymbol{\tau}$  are time-independent. The vector-valued functions in the former space satisfy the boundary condition (4), whereas functions in the latter space satisfy a vanishing normal component at the boundary  $\Gamma_E$ .

The bilinear forms  $a_i : H(\text{div}, \Omega) \times H(\text{div}, \Omega) \rightarrow \mathbb{R}$ ,  $b : H(\text{div}, \Omega) \times L^2(\Omega) \rightarrow \mathbb{R}$ , and  $c : L^2(\Omega) \times L^2(\Omega) \rightarrow \mathbb{R}$  are defined by

$$\begin{aligned} a_i(\boldsymbol{\tau}, \mathbf{h}_i) &:= (\boldsymbol{\tau}, \mathbf{D}_i^{-1} \mathbf{h}_i)_\Omega, \\ b(\boldsymbol{\tau}, m_i) &:= (\text{div } \boldsymbol{\tau}, m_i)_\Omega, \\ c(m_i, v) &:= (m_i, v)_\Omega, \end{aligned}$$

for any  $\boldsymbol{\tau}, \mathbf{h}_i \in H(\text{div}, \Omega)$  and  $m_i, v \in L^2(\Omega)$ .

#### Remarks.

1. When the  $L^2(\Omega)$  space of test functions is replaced by its discrete counterpart, the test function  $v$  is chosen such that it vanishes everywhere in the domain  $\Omega$  except on a given element  $\Omega^e$ . This in turn implies that for  $v$  in (9) set to unity on the element  $\Omega^e$ , one obtains

$$\frac{d}{dt} \int_{\Omega^e} m_i \, d\Omega + \int_{\Omega^e} \text{div } \mathbf{h}_i \, d\Omega = \int_{\Omega^e} f_i \, d\Omega.$$

As a result, such an approximation method is said to have a locally conservative property. That is, the conservation of mass (1) is satisfied on each element.

2. The classification of boundary conditions in the mixed formulation is opposite to the standard single-field case. In the standard formulation, the boundary condition (4) is a natural one as it does not require a priori prescription on the space of trial or test spaces. By contrast, it becomes an essential boundary condition in the mixed formulation since the trial and test functions require the normal flux at the boundary  $\Gamma_E$  to be prescribed a priori. The role of equation (3) is also reversed, that is, it becomes essential in the standard formulation but natural in the mixed formulation.

## 4. Discretisation

The temporal discretisation of the weak formulations, (8) and (9), using a combination of implicit and explicit methods is now presented. Then, the discrete counterparts of the spaces  $H(\text{div}, \Omega)$  and  $L^2(\Omega)$  are detailed in the context of the hierarchical construction of shape functions over a triangular/tetrahedral mesh.

### 4.1. Temporal discretisation

Consider first the temporal discretisation of the mixed formulation using a class of IMEX methods. The time interval of interest is partitioned into subintervals  $[t_{n-1}, t_n]$  with step size  $\Delta t_n = t_n - t_{n-1}$ . Note that the partition need not be uniform, that is, the step-sizes need not be equal. As equation (8) is without a time derivative, we treat it fully implicitly at the current time  $t_n$ . For the IMEX method only the second equation (9) involving time derivatives is relevant. For clarity of notation, we drop the subscript  $i$  from the weak forms (8) and (9), and, in a general multistep context, replace each term by interpolation or extrapolation formulas as linear combinations of previous discrete

values, as defined by

$$\frac{d}{dt} c(\bullet, m) \approx \dot{c}(\bullet) := \frac{\alpha_r}{\Delta t_n} c(\bullet, m^n) + \sum_{j=0}^{r-1} \frac{\alpha_j}{\Delta t_n} c(\bullet, m^{n+j-r}), \quad (10)$$

$$b(\mathbf{h}, \bullet) \approx \widehat{b}(\bullet) := \beta_r b(\bullet, \mathbf{h}^n) + \sum_{j=0}^{r-1} \beta_j b(\mathbf{h}^{n+j-r}, \bullet), \quad (11)$$

$$\ell(\bullet) \approx \tilde{\ell}(\bullet) := \sum_{j=0}^{r-1} \gamma_j \ell^{n+j-r}(\bullet), \quad (12)$$

where  $\ell^k(\bullet)$ ,  $k = n-r, \dots, n-1$ , represents the family of functionals  $\ell(\bullet)$  defined using the time discrete values of the reaction kinetics  $f^k = f(m^k)$ , i.e., with reference to (6),

$$\ell^k(v) = (f^k, v)_\Omega.$$

The coefficients  $\beta_0, \beta_1, \dots, \beta_r$  and  $\alpha_0, \alpha_1, \dots, \alpha_r$  correspond to the implicit interpolation formula (corresponding to equations (10) and (11)) for the value and its time derivative of a field at  $t_n$  on the time interval  $[t_{n-r}, t_n]$ .  $\gamma_0, \gamma_1, \dots, \gamma_{r-1}$  are coefficients of the explicit extrapolation (corresponding to the equation (12)) of a field at  $t_n$  on the interval. The integer  $r$  represents the extent to which previous step solutions, starting from the current step, are included in the scheme.

**Remark 1.** Some of the commonly used IMEX schemes in the literature are:

- IMEX schemes based on the Backward Differentiation Formula (BDF)

Second-order	$\alpha_0 = 1/2, \alpha_1 = -2, \alpha_2 = 3/2,$ $\beta_0 = 0, \beta_1 = 0, \beta_2 = 1,$ $\gamma_0 = -1, \gamma_1 = 2,$
Third-order	$\alpha_0 = 1/24, \alpha_1 = -1/8, \alpha_2 = -7/8, \alpha_3 = 23/24,$ $\beta_0 = 1/16, \beta_1 = -5/16, \beta_2 = 15/16, \beta_3 = 5/16,$ $\gamma_0 = 3/8, \gamma_1 = -5/4, \gamma_2 = 15/8.$

- The second-order Crank-Nicholson – Adams-Bashforth scheme

$$\alpha_0 = 0, \alpha_1 = -1, \alpha_2 = 1,$$

$$\beta_0 = 0, \beta_1 = 1/2, \beta_2 = 1/2,$$

$$\gamma_0 = -1/2, \gamma_1 = 3/2.$$

- The second-order additive Runge-Kutta scheme [37, 38]

$$\alpha_0 = -1, \alpha_1 = 0, \alpha_2 = 1$$

$$\beta_0 = 1, \beta_1 = 0, \beta_2 = 1$$

$$\gamma_0 = 0, \gamma_1 = 2,$$

Substituting the discrete approximations (10)-(12) into the weak formulation (9), together with the discrete equation corresponding to equation (8) at the current time-step renders

$$a^n(\boldsymbol{\tau}) - b^n(\boldsymbol{\tau}) = (\boldsymbol{\tau} \cdot \mathbf{n}, \bar{m})_{\Gamma_N}, \quad \forall \boldsymbol{\tau} \in H(\text{div}, \Omega), \text{ and} \quad (13)$$

$$\dot{c}(v) + \widehat{b}(v) = \tilde{\ell}(v), \quad \forall v \in L^2(\Omega), \quad (14)$$

where

$$a^n(\boldsymbol{\tau}) := a(\boldsymbol{\tau}, \mathbf{h}^n), \quad b^n(\boldsymbol{\tau}) := b(\boldsymbol{\tau}, m^n).$$

Note, equation (13) and (14) constitute a boundary value problem at the time-step  $t_n$ . IMEX methods can be viewed as multistep schemes involving  $r-1$  previous time step's solutions. They are formally  $r$ -order convergent in time.

#### 4.2. Spatial discretisation

Assume a regular decomposition  $\mathcal{T}_h$  of  $\Omega$  into simplexes (triangles in 2D and tetrahedral in 3D). For a given  $k \in \mathbb{Z}^+$  (a non-negative integer), denote the set of all polynomials, on a given  $T \in \mathcal{T}_h$ , whose order is less than or equal to  $k$  by  $\mathcal{P}_k(T)$ . For finite element methods which typically involve the use of non-uniform higher-order approximations on unstructured meshes, increasing the order of the polynomial space locally via  $p$ - and  $hp$ - adaptivity can lead to complications in enforcing global conformity of shape functions [39]. Hierarchical shape functions address such problems, as well as naturally supporting the use of  $p$ - and  $hp$ -adaptivity [40, 41]. The construction of hierarchical shape functions of arbitrary order with various conformity conditions to obtain finite element subspaces for  $L^2(\Omega)$ ,  $H^1(\Omega)$ ,  $H(\text{div}, \Omega)$  on a general unstructured meshes is detailed in Ainsworth and Coyle [39]. An alternative construction of H-div conforming exact sequence element with arbitrary order has been proposed by Fuentes et al. [42]. Note, however, that space in [39] consist of divergence-free zero normal functions was used in following numerical examples in Section 7.

Here, hierarchic shape functions are used to define the finite element spaces corresponding to the triangulation  $\mathcal{T}_h$  such that the test spaces, for concentration  $m$  and flux  $\mathbf{h}$ , are defined as

$$\mathcal{S}_h = \{v_h \in L^2(\Omega) : v_h|_T \in \mathcal{P}^k(T), \text{ where } T \in \mathcal{T}_h\}, \text{ and} \quad (15)$$

$$\mathcal{V}_h^0 = \{\boldsymbol{\tau}_h \in H(\text{div}, \Omega) : \boldsymbol{\tau}_h|_T \in [\mathcal{P}^{k+1}(T)]^{dim} \text{ and } \boldsymbol{\tau}_h \cdot \mathbf{n} = 0 \text{ on } \Gamma_E\}, \quad (16)$$

where  $dim = 1, 2$ , or  $3$  refers to the spatial dimension. While the trial space for concentration  $m$  is also  $\mathcal{S}_h$ , the trial space  $\mathcal{V}_h$  for the flux  $\mathbf{h}$  is given by

$$\mathcal{V}_h = \{\boldsymbol{\tau}_h \in H(\text{div}, \Omega) : \boldsymbol{\tau}_h|_T \in [\mathcal{P}^{k+1}(T)]^{dim} \text{ and } -\boldsymbol{\tau}_h \cdot \mathbf{n} = \bar{h} \text{ on } \Gamma_E\}. \quad (17)$$

It should be noted that to obtain a stable pair  $(m_h, \mathbf{h}_h)$  the order of approximation for  $\mathcal{V}_h$  is required to be at least one order higher than that of  $\mathcal{S}_h$ , see, for example [26].

For the approximation of  $(\mathbf{h}, m)$ , we employ the finite dimensional trial space  $(\mathcal{V}_h, \mathcal{S}_h)$  and test space  $(\mathcal{V}_h^0, \mathcal{S}_h)$ , as defined in equations (15)-(17), following a Galerkin approach. Having specified the corresponding finite element spaces, the spatio-temporal discrete form of the equations (13) and (14) assumes a block matrix system given by

$$\begin{bmatrix} \mathbf{K} & \mathbf{B} \\ \mathbf{B}^T & -\sigma \mathbf{M} \end{bmatrix} \begin{bmatrix} \mathbf{H}^n \\ \mathbf{m}^n \end{bmatrix} = \begin{bmatrix} \mathbf{F} \\ \mathbf{G} \end{bmatrix}, \quad (18)$$

where

$$\mathbf{K}_{IJ} = a(\boldsymbol{\tau}_I^h, \boldsymbol{\tau}_J^h), \quad \mathbf{B}_{IL} = -b(\boldsymbol{\tau}_I^h, v_L^h), \text{ and } \mathbf{M}_{KL} = c(v_K^h, v_L^h).$$

Here,  $I, J$  denote the global indices corresponding to the numbering of the basis elements of  $\mathcal{V}_h$ , while  $K, L$  correspond to that of  $\mathcal{S}_h$ . The right hand side  $\mathbf{F}$  and  $\mathbf{G}$  are given by

$$\mathbf{F}_I = (\boldsymbol{\tau}_I \cdot \mathbf{n}, \bar{m}_h)_{\Gamma_E}, \text{ and}$$

$$\mathbf{G}_K = \frac{1}{\beta_r} \sum_{j=0}^{r-1} [\gamma_j \ell^{n+j-r}(v_K) - \beta_j b(v_K, \mathbf{h}_h^{n+j-r})], \text{ respectively.}$$

The vector  $\mathbf{H}^n$  and  $\mathbf{m}^n$  are the solution vectors containing the degrees of freedom (dof) associated with the current values of  $\mathbf{h}^n$  and  $m^n$ , respectively. The coefficient  $\sigma = \alpha_r / [\Delta t_n \beta_r]$  is a shift coefficient of the mass matrix  $\mathbf{M}$ . The matrices  $\mathbf{K}$  and  $\mathbf{M}$  are positive definite and symmetric. Solvability of the block system (18) also requires that  $\mathbf{B}$  as a linear map is surjective (see, for example, [26] Section 3.3). The requirement that the order of the flux shape function should be at least one order higher than the mass concentration shape function is a sufficient condition for the surjectivity of  $\mathbf{B}$ .

Formally, for sufficiently smooth solutions, the expected rate of convergence for the spatial approximation employing the finite element spaces  $\mathcal{S}_h$  and  $\mathcal{V}_h$  will be of order  $k + 1$  in both the  $L^2$  and the natural norms.

**Remarks.**

1. One of the most important implications of the mixed formulation, from a computational perspective, is that the matrix  $\mathbf{M}$  can be inverted locally on an element-by-element basis, and the inverse is sparse. This is due to the fact that there is no conformity requirement on  $m_h \in \mathcal{S}_h \subset L^2(\Omega)$  over element boundaries.
2. The consequence of the above observation is that one can efficiently solve the block system using a solver that utilises a Schur complement preconditioner. More precisely, one can exactly compute the sparse Schur complement  $\mathbf{S} = \mathbf{K} + \mathbf{B}\mathbf{M}^{-1}\mathbf{B}^T$  in an efficient manner.

## 5. A posteriori error estimators and p-adaptivity

Adaptive finite element methods are a fundamental numerical approach in science and engineering applications. The success of an adaptive algorithm relies on the availability of a good error indicator (or a posteriori error estimator) that provides an upper bound to the true approximation error, and the complexity of its implementation and computation. In this section, we present a residual based error estimate that can be computed cheaply. This estimate together with the hierarchical construction of the shape functions makes the method well suited for local p-adaptivity. Hierarchical shape functions (and dofs) are associated with mesh entities such as vertices, edges, faces, and volumes, rather than nodes. For example, in 2D, if the local order of two adjacent faces  $F_1$  and  $F_2$  sharing an edge  $E$  are different, say order- $k_1$  and order- $k_2$ , respectively, then to satisfy the global  $H(\text{div}, \Omega)$ -conformity one only needs to add local shape functions of order- $\max(k_1, k_2)$  on the edge  $E$ . By contrast, since there is no continuity requirement for  $L^2(\Omega)$  along element interfaces, the shape functions are only associated with faces in the 2D case. Thus, the polynomial order of  $L^2$  shape functions can be set independently in each element, thereby greatly simplifying the implementation of p-adaptivity.

To underpin an effective local p-adaptivity scheme, one requires a reliable a posteriori error estimate that provides an upper bound to the true error and, at best, decays with the same rate as the true error as the polynomial order increases uniformly. The energy norm on  $H(\text{div}, \Omega) \times L^2(\Omega)$ , defined by

$$\|\mathbf{h}\|_{\text{div}, \Omega} + \|m\|_{0, \Omega} \quad (19)$$

is the appropriate norm for measuring the magnitude of approximation errors in the mixed formulation (8) and (9).

To develop the error estimator, and for the sake of simplicity, we shall consider a one-species mixed transient problem with homogeneous boundary condition on  $m_{h,q}$ , where the additional subscript used here is to denote the order of the polynomial space, that is

$$a(\boldsymbol{\tau}_{h,k}, \mathbf{h}_{h,k}^n) - b(\boldsymbol{\tau}_{h,k}, m_{h,k-1}^n) = 0, \quad \forall \boldsymbol{\tau}_{h,k} \in \mathcal{V}_{h,k} \quad (20)$$

$$\sigma c(v_{h,k-1}, m_{h,k-1}^n) + b(\mathbf{h}_{h,k}^n, v_{h,k-1}) = (g, v_{h,k-1})_{\Omega}, \quad \forall v_{h,k-1} \in \mathcal{S}_{h,k-1} \quad (21)$$

where  $g = \tilde{f} - \sigma m_{h,k-1}^{n-1}$ , where  $\tilde{f}$  denotes an extrapolation of  $f$  at the previous time-step values of  $m_h$  that is determined by the specific type of the IMEX scheme, the remaining term in  $g$  is a contribution from temporal discretisation of  $\dot{m}_{h,k-1} = \sigma[m_{h,k-1}^n - m_{h,k-1}^{n-1}]$ . Recall that for stability the orders used in equations (20) and (21) for the flux and mass are  $k$  and  $k-1$ , respectively ( $k > 0$ ). To simplify the notation, in the remainder of this section, the current unknowns  $\mathbf{h}_{h,k}^n$  and  $m_{h,k-1}^n$  are denoted as  $\mathbf{h}_k$  and  $m_{k-1}$ .

### 5.1. Residual and interface jump based error estimates

The a posteriori error estimate corresponding to the energy norm (19) of the error is derived from the following residual and jump based errors. Consider first a sufficiently refined regular mesh  $\mathcal{T}_h$  of  $\Omega$ , where  $h$  is the mesh parameter.

- Element residual errors corresponding to the constitutive and conservation of mass equations: Let  $K$  be an element in  $\mathcal{T}_h$ , define

$$\eta_{K,R,1} := \|\mathbf{D}\nabla m_{k-1} - \mathbf{h}_k\|_{0,K}, \quad (22)$$

$$\eta_{K,R,2} := \|\sigma m_{k-1} + \text{div } \mathbf{h}_k - g\|_{0,K}. \quad (23)$$



- Inter-element interface jump error: Let  $e$  be an edge shared by two adjacent elements  $K^+$  and  $K^-$ , then the jump error is defined by

$$\eta_{e,J} := h^{-1/2} \|\llbracket m_{k-1} \rrbracket\|_{0,e}, \quad (24)$$

where the jump operator is  $\llbracket m_{k-1} \rrbracket = m_{k-1}^+ - m_{k-1}^-$ ,  $m_{k-1}^+$  and  $m_{k-1}^-$  are values of  $m_{k-1}$  at the edge  $e$  from the side of  $K^+$  and  $K^-$ , respectively.

The local error estimate over a given element  $K \in \mathcal{T}_h$  is thus defined by summing the error contributions from (22), (23) and (24),

$$\eta_K := \left[ \eta_{K,R,1}^2 + \eta_{K,R,2}^2 + \sum_{e \in \partial K} \eta_{e,J}^2 \right]^{1/2}, \quad (25)$$

and the global error estimate is given by

$$\eta_{\mathcal{T}_h} := \left[ \sum_{K \in \mathcal{T}_h} [\eta_{K,R,1}^2 + \eta_{K,R,2}^2] + \sum_{e \in \Gamma_h} \eta_{e,J}^2 \right]^{1/2} \quad (26)$$

### 5.2. Upper bound

The global residual error (26) provides an upper bound of the energy norm of the error. To show this, we make use of the following standard estimates

1. Optimality estimate: Let  $(\mathbf{h}, m) \in H(\text{div}, \Omega) \times L^2(\Omega)$  be the exact solution at the current time-step, i.e.,  $t_n$ , then there exists  $C > 0$ , such that

$$\|\mathbf{h} - \mathbf{h}_k\|_{\text{div}, \Omega} + \|m - m_{k-1}\|_{0, \Omega} \leq C \left\{ \inf_{\boldsymbol{\tau}_k \in \mathcal{V}_k} \|\mathbf{h} - \boldsymbol{\tau}_k\|_{\text{div}, \Omega} + \inf_{v_{k-1} \in \mathcal{S}_{k-1}} \|m - v_{k-1}\|_{0, \Omega} \right\} \quad (27)$$

2. Energy norm error estimate of the finite element solution:

$$\begin{aligned} \|\mathbf{h}_k\|_{\text{div}, \Omega} + \|m_{k-1}\|_{0, \Omega} \leq C \left[ \sup_{\substack{\boldsymbol{\tau}_k \in \mathcal{V}_k \\ \|\boldsymbol{\tau}_k\|_{\text{div}, \Omega} = 1}} \{a(\boldsymbol{\tau}_k, \mathbf{h}_k) - b(\boldsymbol{\tau}_k, m_{k-1})\} \right. \\ \left. + \sup_{\substack{v_{k-1} \in \mathcal{S}_{k-1} \\ \|v_{k-1}\|_{0, \Omega} = 1}} \{\sigma c(v_{k-1}, m_{k-1}) + b(\mathbf{h}_k, v_{k-1})\}, \right] \end{aligned} \quad (28)$$

for some  $C > 0$ .

3. *Saturation assumption*: One of the most crucial ingredients towards the proof of an upper bound is the saturation assumption. Roughly, it states that the error norm decreases uniformly as we increase the order of approximation by one. More precisely, let  $(\mathbf{h}_{k+1}, m_k)$  and  $(\mathbf{h}_k, m_{k-1})$  be approximate solutions of (20) and (21), then there is  $0 < \beta < 1$ , such that

$$\|\mathbf{h} - \mathbf{h}_{k+1}\|_{\text{div}, \Omega} + \|m - m_k\|_{0, \Omega} < \beta [\|\mathbf{h} - \mathbf{h}_k\|_{\text{div}, \Omega} + \|m - m_{k-1}\|_{0, \Omega}]. \quad (29)$$

One can construct a mesh  $\mathcal{T}_h$  on which such a saturation estimate does not hold, however, for sufficiently refined regular mesh it always hold true.

Having the above results for the upper bound, it is sufficient to show that the error between successive approximations is bounded from above. That is, there is a constant  $C > 0$  such that

$$\|\mathbf{h}_{k+1} - \mathbf{h}_k\|_{\text{div}, \Omega} + \|m_k - m_{k-1}\|_{0, \Omega} \leq C \eta_{\mathcal{T}_h}. \quad (30)$$

To show this, we first note that

$$a(\boldsymbol{\tau}_{k+1}, \mathbf{h}_{k+1} - \mathbf{h}_k) - b(\boldsymbol{\tau}_{k+1}, m_k - m_{k-1}) = 0, \quad \forall \boldsymbol{\tau}_{k+1} \in \mathcal{V}_{k+1} \quad (31)$$

$$\sigma c(v_k, m_k - m_{k-1}) + b(\mathbf{h}_{k+1} - \mathbf{h}_k, v_k) = 0. \quad \forall v_k \in \mathcal{S}_k \quad (32)$$

Hence, by the estimate (28), we have, for some  $C > 0$ ,

$$\begin{aligned}
& \|\mathbf{h}_{k+1} - \mathbf{h}_k\|_{\text{div}, \Omega} + \|m_k - m_{k-1}\|_{0, \Omega} \\
& \leq C \left[ \sup_{\substack{\boldsymbol{\tau}_{k+1} \in \mathcal{V}_{k+1} \\ \|\boldsymbol{\tau}_{k+1}\|_{\text{div}, \Omega} = 1}} \{a(\boldsymbol{\tau}_{k+1}, \mathbf{h}_{k+1} - \mathbf{h}_k) - b(\boldsymbol{\tau}_{k+1}, m_k - m_{k-1})\} \right. \\
& \quad \left. + \sup_{\substack{v_k \in \mathcal{S}_k \\ \|v_k\|_{0, \Omega} = 1}} \{\sigma c(v_k, m_k - m_{k-1}) + b(\mathbf{h}_{k+1} - \mathbf{h}_k, v_k)\} \right].
\end{aligned} \tag{33}$$

Now, since

$$a(\boldsymbol{\tau}_k, \mathbf{h}_{k+1} - \mathbf{h}_k) - b(\boldsymbol{\tau}_k, m_k - m_{k-1}) = 0, \quad \forall \boldsymbol{\tau}_k \in \mathcal{V}_k, \tag{34}$$

it follows for every  $\boldsymbol{\tau}_k$  that

$$\begin{aligned}
& a(\boldsymbol{\tau}_{k+1}, \mathbf{h}_{k+1} - \mathbf{h}_k) - b(\boldsymbol{\tau}_{k+1}, m_k - m_{k-1}) \\
& = a(\boldsymbol{\tau}_{k+1} - \boldsymbol{\tau}_k, \mathbf{h}_{k+1} - \mathbf{h}_k) - b(\boldsymbol{\tau}_{k+1} - \boldsymbol{\tau}_k, m_k - m_{k-1}) \\
& = -a(\boldsymbol{\tau}_{k+1} - \boldsymbol{\tau}_k, \mathbf{h}_k) + b(\boldsymbol{\tau}_{k+1} - \boldsymbol{\tau}_k, m_{k-1}) \\
& = \sum_K \left\{ (\boldsymbol{\tau}_{k+1} - \boldsymbol{\tau}_k, \mathbf{h}_k)_K + (\text{div}(\boldsymbol{\tau}_{k+1} - \boldsymbol{\tau}_k), m_{k-1})_K \right\} \\
& = \sum_K \left\{ -(\boldsymbol{\tau}_{k+1} - \boldsymbol{\tau}_k, \mathbf{h}_k)_K + (\boldsymbol{\tau}_{k+1} - \boldsymbol{\tau}_k, \nabla m_{k-1})_K \right\} + \sum_{e \in \Gamma_h} ([\boldsymbol{\tau}_{k+1} - \boldsymbol{\tau}_k] \cdot \mathbf{n}, \llbracket m_{k-1} \rrbracket)_e \\
& = \sum_K (\boldsymbol{\tau}_{k+1} - \boldsymbol{\tau}_k, \mathbf{h}_k - \nabla m_{k-1})_K + \sum_{e \in \Gamma_h} ([\boldsymbol{\tau}_{k+1} - \boldsymbol{\tau}_k] \cdot \mathbf{n}, \llbracket m_{k-1} \rrbracket)_e \\
& \leq \sum_K \|\boldsymbol{\tau}_{k+1} - \boldsymbol{\tau}_k\|_{0, K} \|\mathbf{h}_k - \nabla m_{k-1}\|_{0, K} + \sum_{e \in \Gamma_h} \|[\boldsymbol{\tau}_{k+1} - \boldsymbol{\tau}_k] \cdot \mathbf{n}\|_{0, e} \|\llbracket m_{k-1} \rrbracket\|_{0, e} \\
& = \sum_K \eta_{K, R, 1} \|\boldsymbol{\tau}_{k+1} - \boldsymbol{\tau}_k\|_{0, K} + \sum_{e \in \Gamma_h} \eta_{e, J} h^{1/2} \|[\boldsymbol{\tau}_{k+1} - \boldsymbol{\tau}_k] \cdot \mathbf{n}\|_{0, e}.
\end{aligned}$$

Hence, we obtain that

$$\sup_{\substack{\boldsymbol{\tau}_{k+1} \in \mathcal{V}_{k+1} \\ \|\boldsymbol{\tau}_{k+1}\|_{\text{div}, \Omega} = 1}} \{a(\boldsymbol{\tau}_{k+1}, \mathbf{h}_{k+1} - \mathbf{h}_k) - b(\boldsymbol{\tau}_{k+1}, m_k - m_{k-1})\} \leq C_1 \left\{ \sum_K \eta_{K, R, 1}^2 + \sum_e \eta_{e, J}^2 \right\}^{1/2} \tag{35}$$

for some constant  $C_1 > 0$ . A similar argument also leads to

$$\sup_{\substack{v_k \in \mathcal{S}_k \\ \|v_k\|_{0, \Omega} = 1}} \{\sigma c(v_k, m_k - m_{k-1}) + b(\mathbf{h}_{k+1} - \mathbf{h}_k, v_k)\} \leq C_2 \left\{ \sum_K \eta_{K, R, 2}^2 \right\}^{1/2}. \tag{36}$$

Therefore, for  $C = \max(C_1, C_2)$  we obtain the estimate (30). Employing the saturation estimate (29) and (30), it then follows that

$$\|\mathbf{h} - \mathbf{h}_k\|_{\text{div}, \Omega} + \|m - m_{k-1}\|_{0, \Omega} \leq \frac{C}{1 - \beta} \eta_{\tau_h}. \tag{37}$$

Here the constant  $C$  depends only on the approximation order  $k$  and  $h$ .

## 6. Adaptive p-refinement strategy

Once the problem is solved with a given distribution of polynomial orders over the mesh entities, and the local a posteriori error  $\eta_K$  over each element  $K \in \mathcal{T}_h$  is calculated, the next step is to apply a p-refinement strategy inspired by the well-known bulk-chasing Dörfler's criterion [43]. The refinement algorithm is characterised by two parameters  $\theta_{\min}$  and  $\theta_{\max}$ , where  $0 \leq \theta_{\min} < \theta_{\max} \leq 1$ , and is performed in three stages:

**Stage 1.** Given a posteriori error estimate  $\eta_K$  on each element  $K \in \mathcal{T}_h$  and  $\eta_{\text{MAX}} = \max_{K \in \mathcal{T}_h} \{\eta_K\}$ , the polynomial order over element  $K$  is raised by one if

$$\eta_K \geq \theta_{\text{max}} \eta_{\text{MAX}},$$

or reduced by one if

$$\eta_K \leq \theta_{\text{min}} \eta_{\text{MAX}}.$$

After applying this first stage of the adaptive process it may happen that the polynomial order distribution over adjacent elements be greater than one order. Numerical experiments (not presented here) revealed that heterogeneity of polynomial order distribution results in undesirable oscillatory feature of the approximated solution. Hence, following this step, certain smoothing of polynomial order over the mesh is required, which leads us to the next stage.

**Stage 2.** To smooth the polynomial order distribution, we force the difference in polynomial order between two adjacent elements  $K$  and  $K'$  to not exceed one, by resetting the order on the element with smaller degree to that of with the higher degree minus one. That is, suppose  $\text{order}(K) + 1 < \text{order}(K')$ , then we reset  $\text{order}(K) := \text{order}(K) - 1$ .

**Stage 3.** This stage is responsible to maintain the  $H(\text{div})$ -conformity of the space of flux functions after we execute the above two stages. For each interface entity  $E$  shared by two elements  $K$  and  $K'$ , we set the order as the maximum of the polynomial orders over  $K$  and  $K'$ .

The adaptive p-refinement algorithm consisting of the above three stages is summarised in Algorithm 1. Following the above p-adaptive stages, one also needs to adjust the quadrature rules over the mesh entities appropriately in order to match the polynomial order distributions optimally.

---

**Algorithm 1:** Adaptive p-refinements algorithm

---

**Input:**  $\eta_K$  on each  $K \in \mathcal{T}_h$ ,  $\theta_{\text{max}}$  and  $\theta_{\text{min}}$

**Stage 1.** Setting order on each  $K$ ;

**for**  $K \in \mathcal{T}_h$  **do**

**if**  $\eta_K \geq \theta_{\text{max}} \eta_{\text{MAX}}$  **then**

        raise polynomial order on  $K$  by one;

**end**

**if**  $\eta_K \leq \theta_{\text{min}} \eta_{\text{MAX}}$  **then**

        decrease polynomial order on  $K$  by one but not less than a minimum order, say 1;

**end**

**end**

**Stage 2.** Order smoothing;

**for**  $E \in \Gamma_h$  *shared by two elements  $K$  and  $K'$  in  $\mathcal{T}_h$  such that the order in  $K$  is greater than that of  $K'$  by more than 1* **do**

    set: order in  $K'$  equals order in  $K$  minus 1;

**end**

**Stage 3.** Setting order on the interfaces;

**for**  $E \in \Gamma_h$  **do**

**if**  $E$  is on the boundary with only one adjacent element  $K$  **then**

        set order on  $E$  to be equal to that of on  $K$ ;

**else**

        find adjacent elements  $K$  and  $K'$  sharing  $E$ ;

        Set order on  $E$  to be maximum of orders on  $K$  and  $K'$ ;

**end**

**end**

---

## 7. Numerical examples

Two groups of numerical examples are presented: the first compares the convergence of results of the mixed scheme and the standard single-field formulation in approximating important aspects of the solution. These include solutions involving singularities, and computation of the speed of travelling wave solutions. Suitability of the p-adaptive mixed formulation in terms of the features of the solution is also investigated. The second group showcases the capabilities of the p-adaptive, IMEX mixed formulation in simulating problems of practical importance: pattern formation and electrophysiology. We investigated several IMEX schemes, for the examples presented in this section we opted for the second-order additive Runge-Kutta scheme.

The computer implementation of the proposed numerical scheme is carried out using the open-source library MOFEM [44]. The library integrates and utilises other open-source libraries such as MOAB, a mesh-oriented database [45, 46], and PETSc [47, 48]. The MOAB library is used to store and manage mesh related data, while PETSc is used for parallel operations involving linear algebra.

The IMEX methods presented in Section 4 are implemented using the PETSc (Portable, Extensible Toolkit for Scientific computations [47, 48]) time solvers [49].

### 7.1. Convergence tests

Two cases are considered. In the first, a spatially smooth solution is considered with a piece-wise temporal profile that stabilises after some specified time. Thus, the approximation error after a sufficiently long simulation time is associated entirely with the spatial discretisation. The second case considers the approximation of a one-species Fisher's type problem on a square domain  $\Omega$  with heterogeneous diffusivity.

#### a) Smooth manufactured solution

It is well-known that both standard and the mixed finite element formulations are optimal in terms of convergence in the  $L^2$ -norm, i.e.,  $\mathcal{O}(h^{p+1})$ , for sufficiently smooth solutions, where  $p$  is the order of the finite element space. Noting that the mesh size parameter  $h$  is inversely proportional to the number of degrees-of-freedom to the power  $dim$ , where  $dim = 1, 2$  or  $3$  is the space dimension, these optimality results are confirmed practically, as shown in Fig. 2, by considering a manufactured solution based on the smooth function

$$g(x, y) = 1 + \sin(2\pi x) \sin(2\pi y), \quad \text{for } (x, y) \in \Omega. \quad (38)$$

Consider first a one-species reaction-diffusion system over the domain  $\Omega = [-1, 1]^2$  (so that  $g$  vanishes on the boundary) with isotropic diffusivity  $\mathbf{D} = d\mathbf{I}$ ,  $d = 1$ , and then assume the exact (manufactured) solution for the mass concentration  $m$

$$m(x, y, t) = \begin{cases} t g(x, y), & t < t^*, \\ g(x, y), & t \geq t^*. \end{cases} \quad (39)$$

for some given  $t^*$ . The right-hand-side source term  $f$  is given by the residual of the exact solution, i.e.,

$$f := \dot{m} + \text{div}(\mathbf{D}\nabla m).$$

Note that  $\dot{m}$  and  $\text{div}(\mathbf{D}\nabla m)$  are also piecewise in time, i.e.,

$$\dot{m} = \begin{cases} g(x, y), & t < t^*, \\ 0, & t > t^*, \end{cases} \quad \text{and} \quad \text{div}(\mathbf{D}\nabla m) = \begin{cases} t \text{div}(\mathbf{D}\nabla g), & t < t^*, \\ \text{div}(\mathbf{D}\nabla g), & t \geq t^*. \end{cases}$$

Consequently, the source term is also temporally piece-wise which stabilises to a time-independent profile after  $t^*$ . Note also that for  $t < t^*$ ,  $\bar{m} = t$  on the boundary  $\Gamma$ , and for  $t > t^*$ ,  $\bar{m} = 1$ . With this set up, the temporal discretisation error after a time  $t$  sufficiently greater than  $t^*$  will be negligible, and the total error is dominated by the spatial approximation. In other words, it amounts to the approximation of the steady state case ( $\dot{m} = 0$ ) with the manufactured solution  $m = g$ .

The convergence results presented in Fig. 3 and 4 are obtained by a successive refinement of an initial uniform mesh with  $h = 2/5$ , and the inflection time  $t^*$  and a uniform time step length  $\Delta t$  are chosen to be 1 and 0.1, respectively,

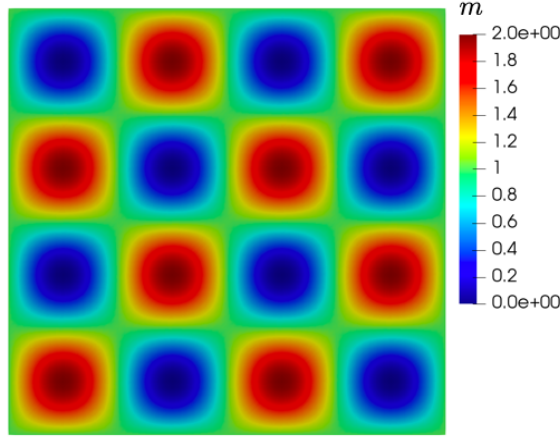


Figure 2: Exact (manufactured) solution for  $m$  at  $t = 1$ .

corresponding to each mesh. The simulations are run up to  $t = 10$ ; a sufficiently long time to ensure that the temporal discretisation error is negligible.

With the same construction of the manufactured solution (39), the convergence rate of the mixed formulation with respect to the  $H^1$ -norm, given by

$$[\|m - m^h\|_{0,\Omega}^2 + \|\mathbf{h} - \mathbf{h}^h\|_{0,\Omega}^2]^{1/2},$$

is expected to be one order higher than that of the standard formulation, as demonstrated in Fig. 4. This is due to the fact that the flux  $\mathbf{h}_h$  for the standard formulation is obtained by postprocessing from  $m_h$ , unlike the mixed formulation, wherein the flux is directly approximated as a primary field variable.

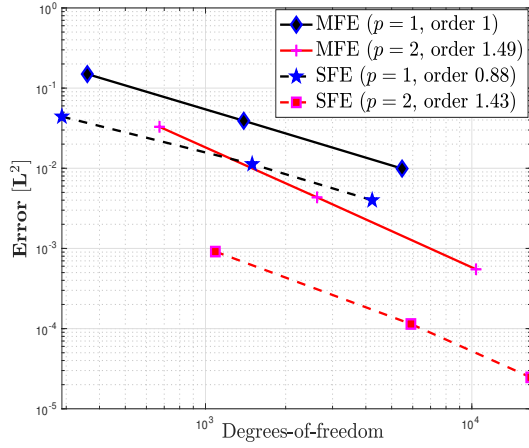
The next set of examples in this group aims at demonstrating the effectiveness of the p-adaptive mixed formulation in resolving fine features of solutions efficiently. For smooth solutions such as (38), the variability of the solution is almost uniform on the larger scale. In this case, the application of p-adaptivity is less effective since the error is distributed almost uniformly. This is demonstrated in the convergence result displayed in Fig. 5. It shows that the p-adaptive strategy with parameters  $\theta_{\min} = 0.02$  and  $\theta_{\max} = 0.8$ , representing a quite conservative adaptive strategy, produces a convergence trend which is not generally better than that of the uniform p-refinement. As expected, at each adaptive step, as shown in Fig. 6, the error is distributed almost uniformly, which leads to the marking of most of the elements for refinement. This corresponds to the convergence result shown in Fig. 6, which is not better than the uniform p-adaptive strategy.

In contrast, when the solution is characterised by the presence of sudden spatial changes over the domain, such as travelling waves, the p-adaptive algorithm becomes most effective. To demonstrate this, we consider a smooth analytical solution (manufactured) replacing the  $g$  in equation (38) by the bump function over the square domain  $\Omega = [-1, 1]^2$ ,

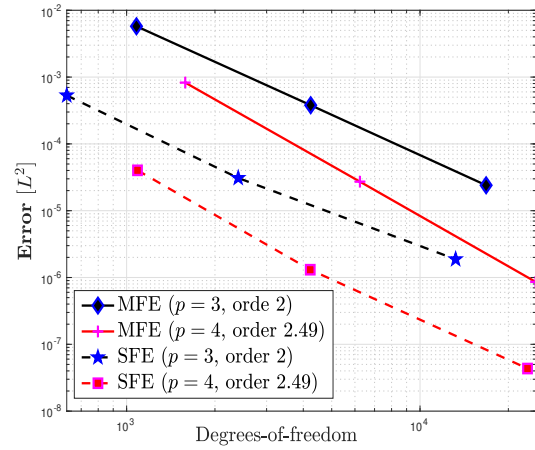
$$g(x, y) = \begin{cases} \exp\left(\frac{-x^2 - y^2}{r^2 - x^2 - y^2}\right) & \text{if } x^2 + y^2 < r^2, \\ 0 & \text{otherwise.} \end{cases} \quad (40)$$

where  $r = 0.75$ . As in the previous examples, the diffusion parameter is chosen such that  $d = 1$ , and  $t^* = 1$  and  $\Delta t = 0.1$ . The error is computed at  $t = 10$ , as in the previous simulation, as it is far enough from the inflection time  $t^* = 1$  so that the temporal discretisation error becomes negligible. The spatial mesh is unstructured and relatively coarse. It can be easily seen that the bump function is infinitely many times differentiable hence smooth. However, as can be seen from Fig. 7, along the circle  $x^2 + y^2 = r^2$  the solution changes drastically from zero to some finite non-zero value within a relatively small distance in the radial direction.

Thus it is expected that most of the error of the finite element approximation concentrates along the circle. This becomes evident in the distributions of the error as well as polynomial order over the mesh as displayed in the p-

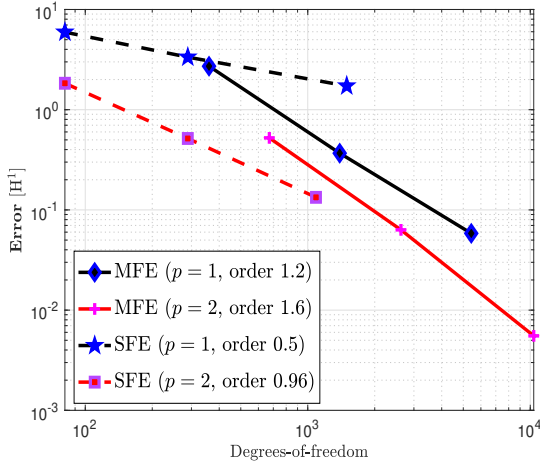


(a)

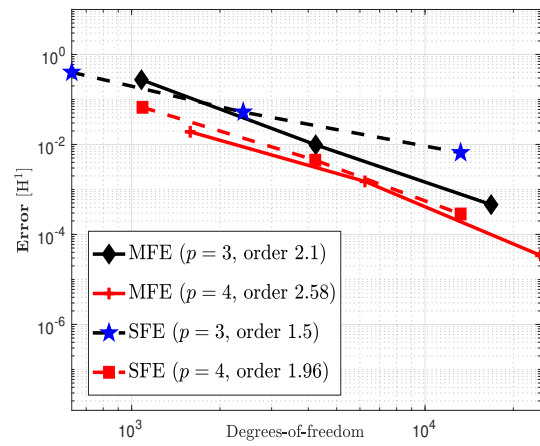


(b)

Figure 3: Comparison of convergence rates of the mixed (MFE) and standard (SFE) formulations with respect to the  $L^2$  error norm. Figure (a) is for orders of approximation  $p = 1, 2$ , while (b) is for  $p = 3, 4$ . The legend 'order' stands for the absolute value of the slope of the convergence curve once a consistent slope is established between consecutive refinements.



(a)



(b)

Figure 4: Comparison of convergence rate the mixed (MFE) and standard (SFE) formulations with respect to the  $H^1$ -norm. Figure (a) is for order of approximation  $p = 1, 2$ , for  $m$  while (b) is for  $p = 3, 4$ . The legend 'order' stands for the absolute value of the slope of the convergence curve once a consistent slope is established between consecutive refinements.

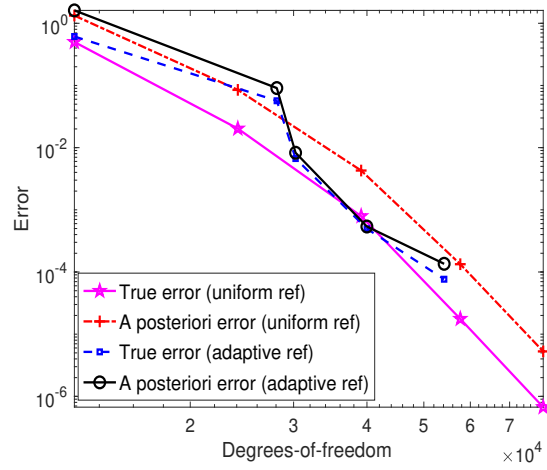


Figure 5: Comparison of the p-adaptive and uniform refinement strategies for smooth and slowly varying solution.

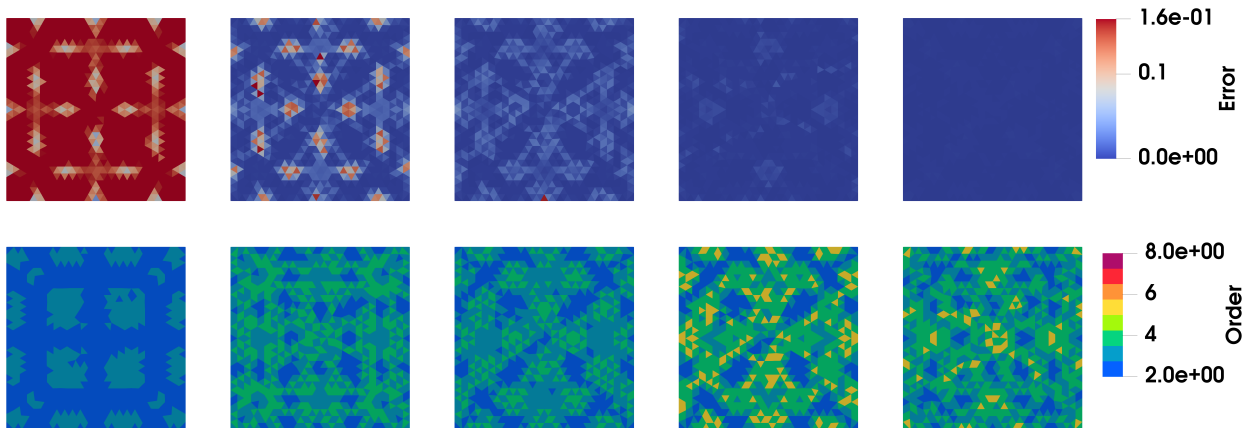


Figure 6: Distribution of error and polynomial order over the mesh at each p-adaptive iteration

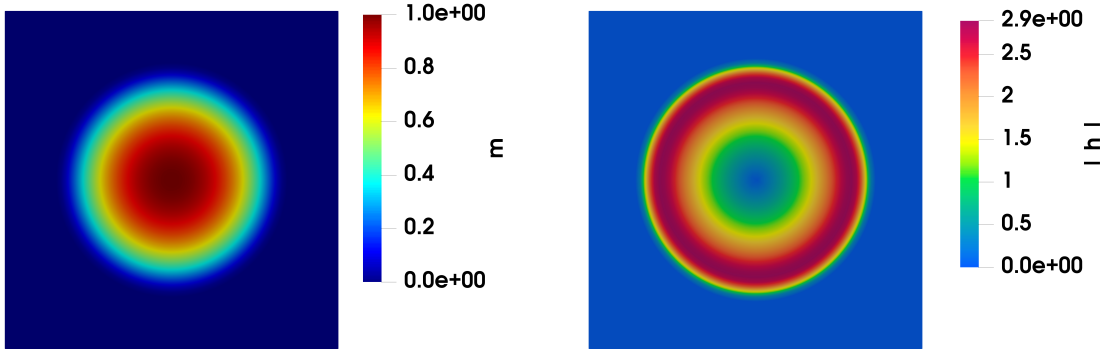


Figure 7: Bump function (left) and norm of the gradient (right)

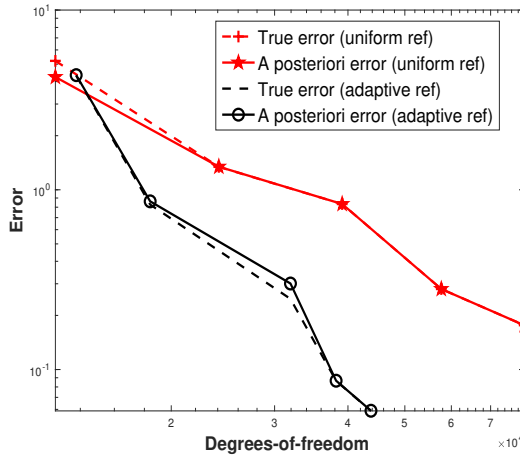


Figure 8: Convergence comparison between uniform and adaptive p-refinements for the bump function solution.

adaptive sequence as shown in Fig. 9. The corresponding convergence result, shown in Fig. 8, exhibits the better performance compared to the uniform p-adaptive strategy.

#### Rough solution with singularities

Consider a one-species reaction diffusion problem on the square domain  $\Omega = [-1, 1]^2$ , with reaction kinetics of Fisher's type,

$$f = m[1 - m]. \quad (41)$$

The domain is comprised of square patches with contrasting diffusivities  $\mathbf{D} = d(\mathbf{x})\mathbf{I}$  with a checkerboard pattern, as shown in Fig. 10 (a). For the blue patches  $d = 0.1$  and for the remaining patches  $d = 0.001$ . An initial condition of  $m^0 = 0.5$  on the centre square and zero elsewhere is prescribed - see Fig. 10 (b). A homogeneous flux boundary condition of the type given in equation (4) is prescribed along the entire boundary  $\Gamma$  (i.e.,  $\bar{h} = 0$ ).

Solutions were computed up to  $t = 6$  with a time-step size  $\Delta t_n = 0.1$ . Both the standard and mixed solutions were computed and compared. Because of the heterogeneous diffusivity, the solution develops kinks along the interfaces of the patches and singularities at the corners. It is important to note the well-known fact that such irregularities (singularities) cannot be resolved by increasing the polynomial order. A feasible way of resolving such features is using local h-adaptivity. In fact, numerical experimentation (not presented here) showed that p-adaptivity caused



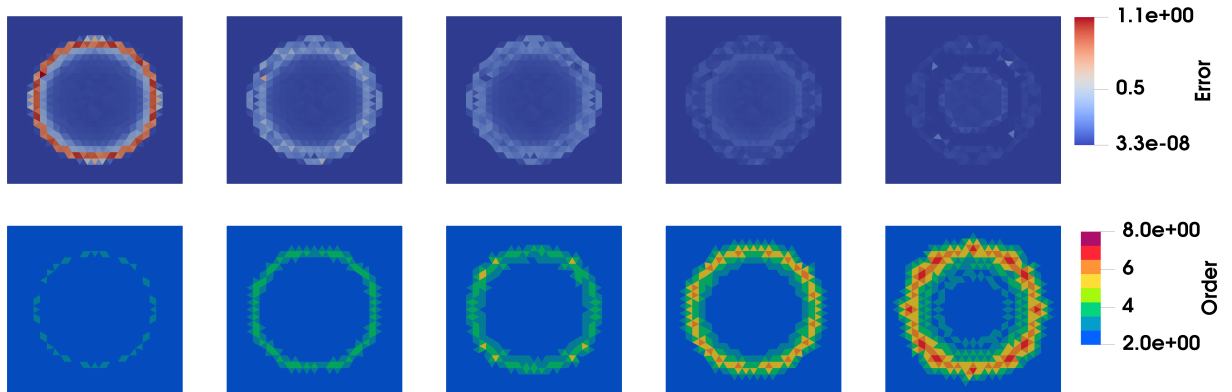


Figure 9: Distribution of the error (top row) and polynomial order (bottom row) in a p-adaptive sequence.

artificial oscillation near the corners as the polynomial order increases locally. For example, Fig. 11 (b) shows the distribution of the flux magnitude, computed using the mixed method with the a priori adaptively refined mesh as shown in Fig. 11 (a). Figs. 11 (c) and (d) show the mass distribution computed using the standard and mixed methods, respectively. Even though the reference mesh Fig. 11 (a) has been used in both cases, the difference in their respective solutions is apparent. This is due to the fact that the standard formulation uses a  $H^1$ -conforming space and is unable to approximate solutions with features such as discontinuities and singularities. By contrast, the mixed formulation uses a non-conforming  $L^2(\Omega)$  space for  $m^h$  and the exact, physically motivated conformity for the flux  $\mathbf{h}^h$ , i.e.,  $H(\text{div})$ . This allows the mixed method to capture such features.

Fig. 12 shows the superiority of the mixed method over the standard single-field formulation. Here, the mass profiles along a line segment, coloured in red in Fig. 11 (a), that connects the centre and the right top corner of the square domain  $\Omega$  are displayed. Along this line segment, there are two interior corners of patches where discontinuities in  $m_h$  are expected. The solutions were obtained using various meshes at different levels of refinement with parameter  $h = 1/5, 1/10, 1/20$ , and  $1/40$ , including a reference mesh (denoted by Ref. Mesh), which is obtained by refining along the interfaces and corners of the patches. The discontinuities at the interior corners are captured almost exactly using the mixed method regardless of the refinement level. By contrast, using the standard formulation, none of the meshes resulted in a reasonable approximation of the discontinuities. Another interesting observation is that the approximation of the mixed formulation converges from below. This is opposite to the standard formulation in which the approximation overestimates the solution.

## 7.2. Speed of travelling wave solutions

The one-species Fisher-type equation (41) supports travelling wave solutions. The wave nature of the solution depends on the relative size of the reaction and diffusion terms. When the reaction term is dominant, the wave front steepens and the wave travels with a finite speed. By contrast, when diffusion is dominant, the influence of the reaction term becomes less and the solution exhibits typical diffusion behaviour, that is, it decays exponentially.

Consider the planar domain as shown in Fig. 13, composed of rectangular patches that are arranged horizontally with increasing diffusivity between successive patches. The rectangular domain has height 0.8 and the width of the 5 patches are 0.6, 0.4, 0.4, 0.4, and 2.2. The maximum diffusivity  $d = 0.5$  is chosen so that the problem remains in the wave propagation regime. As the initial condition, the mass concentration  $m = 1$  is set on the first one-third of the left-most patch, while on the rest of the domain  $m$  is set to zero at  $t = 0$ . Since the diffusivity is smallest in the first left patch, the solution starts to evolve slowly with a sharp wave front. As the wave passes each interface its speed

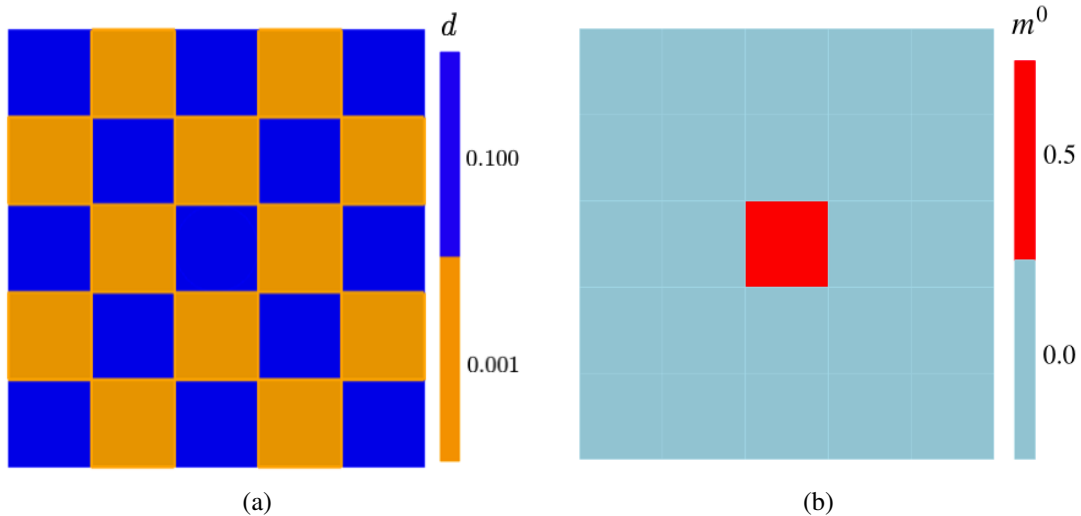


Figure 10: The heterogeneous domain  $\Omega = [-1, 1]^2$  with a checkerboard pattern where in (a) the blue regions have  $d = 1 \times 10^{-3}$  and the rest have  $d = 1 \times 10^{-1}$ , and in (b) an initial value  $m^0 = 0.5$  is prescribed.

increases while the sharpness of the wavefront decreases. The wavefront is identified using a levelset method based on a mass concentration value of 0.6. Uniform time steps of length  $\Delta t = 0.05$  have been used. The position of the wavefront against time is presented in Fig. 14 for various levels of mesh refinement. Importantly, the approximations based on the mixed method are accurate and converge to the correct wave speed. However, the approximation using the standard method initially overestimates the true speed of the travelling wave solution, and only slowly converges to the correct speed. The p-adaptive mixed formulation is used with the second coarsest mesh, and it is also obtained that the speed of the wave is in good agreement with that of the converged results of the mixed or standard methods.

### 7.3. Pattern formation in ecological applications

The class of problems considered here have application in various important areas including biological pattern formation, morphogenesis [2] and electrophysiology [50].

#### Segregation pattern

A competition-diffusion model involving three interacting species is considered. The level and mode of interaction between the species is the same. This, in effect, means that the magnitude of each species that is consumed by the others is the same as the other species that consumes it. The reaction term, for each  $i = 1, 2, 3$ , is given by

$$f_i = m_i[1 - a_{i1}m_1 - a_{i2}m_2 - a_{i3}m_3], \quad (42)$$

where the parameters in the model are represented in Table 1. It is assumed that all the three species have the same mobility rates, i.e.,  $\mathbf{D} = d\mathbf{I}$ , where  $d = 0.01$ . In cases where the dynamics is largely influenced by the reaction term, it is important to analyse the local stability of the spatially homogeneous problem (i.e., ignoring the diffusion terms). Such an analysis provides important insights into the range of parameter values for various possible spatio-temporal interaction patterns. A local stability analysis of the problem described by equations (42) reveals eight equilibrium points of which only, namely  $[m_1, m_2, m_3]_1 = [1/a_{11}, 0, 0]$ , and  $[m_1, m_2, m_3]_2 = [0, 1/a_{22}, 0]$ , and  $[m_1, m_2, m_3]_3 = [0, 0, 1/a_{33}]$  are quasi-stable. In the case of the segregation problem, these equilibrium points represent regions which are exclusively occupied by one of the species.

It is assumed initially that all the three species are distributed randomly over the domain  $\Omega = [-1, 1]^2$  as shown in Fig. 15. Such problems have been studied previously [25, 51, 52]. In those studies the numerical approaches were either the finite difference method or the standard finite element method.

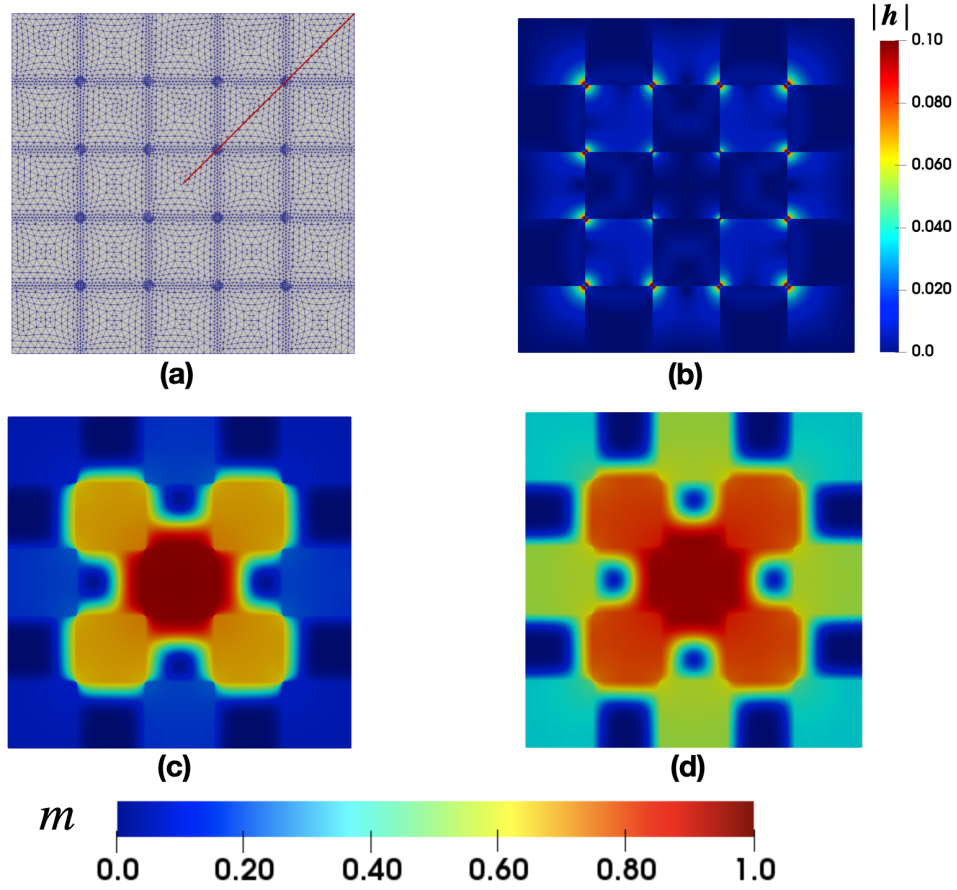


Figure 11: Comparison of approximations by standard and mixed methods, (a) an a priori adaptively refined mesh on which the mass concentration approximation at  $t = 6$  are computed based on the standard (c) and mixed (d) methods. (b) shows the distribution of magnitude of flux, computed using the mixed method using the mesh (a) at  $t = 6$ , where singularities at the corners of the patches are shown.

Table 1: List of parameters for three species segregation problem

$d_1$	$d_2$	$d_3$	$a_{11}$	$a_{12}$	$a_{13}$	$a_{21}$	$a_{22}$	$a_{23}$	$a_{31}$	$a_{32}$	$a_{33}$
0.01	0.01	0.01	1	3	3	3	1	3	3	3	1

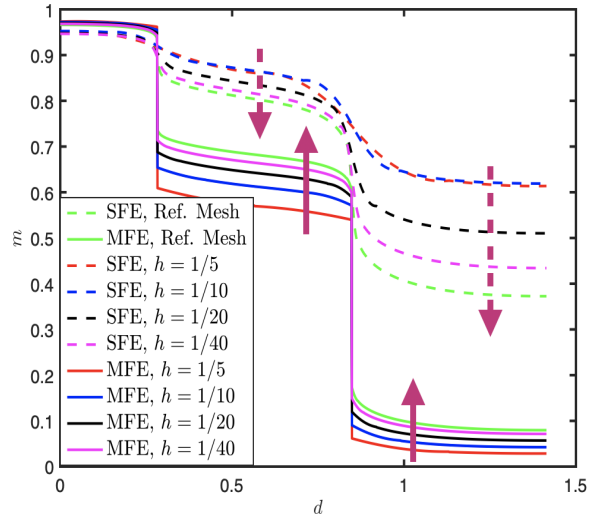


Figure 12: Mass concentration profile along a diagonal line from the centre of the square to the right corner (as indicated in Fig. 11(a) with a red line segment) at  $t = 6$ . Various uniform meshes at different refinement levels described by the mesh parameter  $h$  along with a reference mesh (designated as Ref. Mesh), which was adaptively refined along the interfaces and corners of the patches, were used.

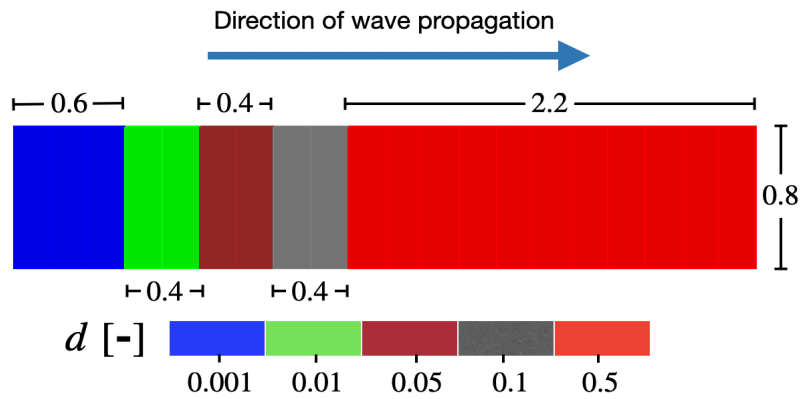


Figure 13: Domain for the travelling wave problem. Color indicates the diffusivity, which is piecewise constant and increasing towards the right.

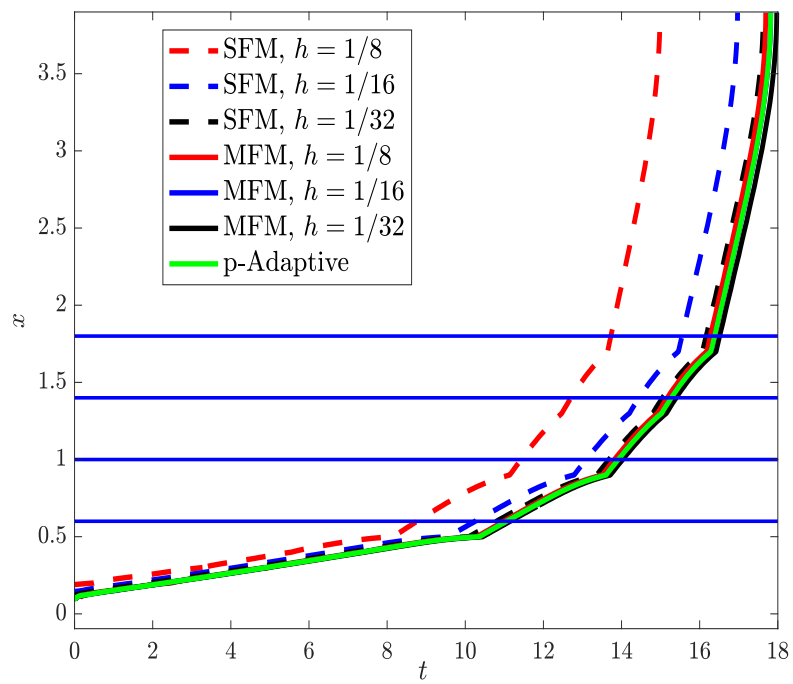


Figure 14: Comparison of speed of travelling wave solution with time. The broken lines correspond to the computation using the standard formulation (SFM) while the solid lines correspond to the mixed formulation (MFM).

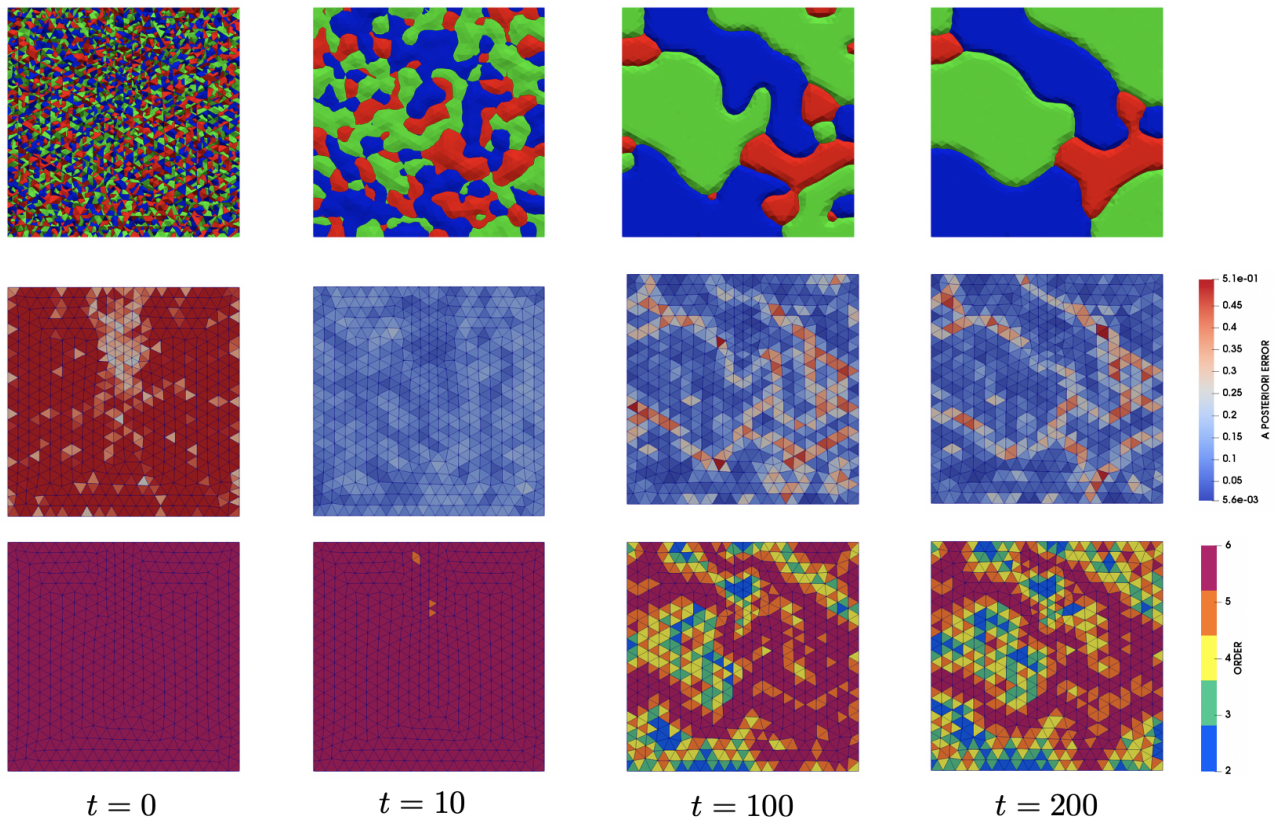


Figure 15: Development of segregation pattern as a result of interactions of the three species (Equation (42), Table 1) at various times. The blue color surface plot represents the region dominated by  $m_1$  (i.e.,  $m_1 > m_2$  and  $m_1 > m_3$ ), red color surface plot by  $m_2$ , and yellow surface plot by  $m_3$ .

Table 2: List of parameters for three species cyclic interaction problem

$d_1$	$d_2$	$d_3$	$a_{11}$	$a_{12}$	$a_{13}$	$a_{21}$	$a_{22}$	$a_{23}$	$a_{31}$	$a_{32}$	$a_{33}$
0.01	0.01	0.01	1	2	7	7	1	2	2	7	1

A relatively coarse mesh for such a problem is used, but to sufficiently represent the random initial condition and to capture the fast dynamics at the beginning stage order 6 polynomial approximation are used as shown in the lower left corner of Fig. 15. During the early stages of evolution, as shown in Fig. 15 at  $t = 0$  through  $t = 10$ , the dynamics appears to be reasonably fast. Eventually, as shown in the second row of Fig. 15, as the species start to establish themselves into well defined regions each occupied by one of the species, the interaction starts to proceed in a slower manner. During this time the error distribution becomes more concentrated in the vicinity of the boundaries of these regions. It is shown that the polynomial adaptation follows the error distribution very closely. These regions tend to a quasi-stable configuration, that is patches of convex shapes with triple junctions with angle of separation given by  $2\pi/3$ .

#### Cyclic interaction

Here a three-species competition-diffusion system of equations with the reaction term given by equation (42) is considered. The species react with each other in a cyclic way (based on parameters in Table 2) resulting in various complex spatio-temporal patterns such as spiral-like, and band-like structures depending on the topology of the habitat and the initial configuration.

A square habitat  $\Omega = [-1, 1]^2$  is considered with initial configuration as shown in Fig. 16 at  $t = 0$  (top row left). The parameter values considered in the simulations are presented in Table 2. A relatively coarse mesh is used for such problem whose solution have complex, fine and spiral structure. A uniform time stepping is also used with step size  $\Delta t = 0.2$ . Initially the polynomial order is set to 2 and adaptively increases to 6 (with parameter  $\theta_{\max} = 0.6$  and  $\theta_{\min} = 0.1$ ) throughout the simulation. As shown in Fig. 16, a spiral pattern starts to form turning in a clockwise direction. The spiral shape consists of stripes of each species lying side-by-side, and eventually fills the region and continues with the same spiral feature. It is also shown that the error is high in the vicinity of the interface between the species which led to the adaptivity taking place only on elements around such interfaces. This clearly shows the efficiency of the p-adaptive mixed method.

#### 7.4. Spiral wave re-entry in electrophysiology

The propagation of ionic current in the cardiac muscle can be simulated using a monodomain model, which is mathematically equivalent to the reaction-diffusion equation. The transmembrane electric potential can be viewed as a diffusing species, which “reacts” locally with the cellular ion channel densities. The reaction term depends on the ion channel densities through a set of highly nonlinear and coupled ordinary differential equations. Thus, the ion channel densities can be viewed as non-diffusing species and treated simply as internal state variables. There are a large number of models available for the reaction term (called cardiac electrophysiology models) with varying degrees of complexity in terms of the number of (internal) variables. Using the proposed mixed method, we simulate the phenomenon of spiral wave re-entry — the cause of several cardiac arrhythmias, such as ventricular tachycardia, atrial flutter, and atrial and ventricular fibrillation.

A square block of cardiac tissue of dimension 100 mm is considered. The domain is subdivided into a relatively coarse triangular mesh. The propagation of the transmembrane electric potential (more commonly known as the action potential) is governed by

$$\frac{d}{d\tau}m - \operatorname{div}(\mathbf{D}\nabla m) = f(m, r) + I_{\Omega'}(\tau), \quad (43)$$

where the non-dimensional variable  $m \in [0, 1]$  is related to the transmembrane action potential  $E$  [mV] through the relation

$$E = [100m - 80] \text{ mV},$$

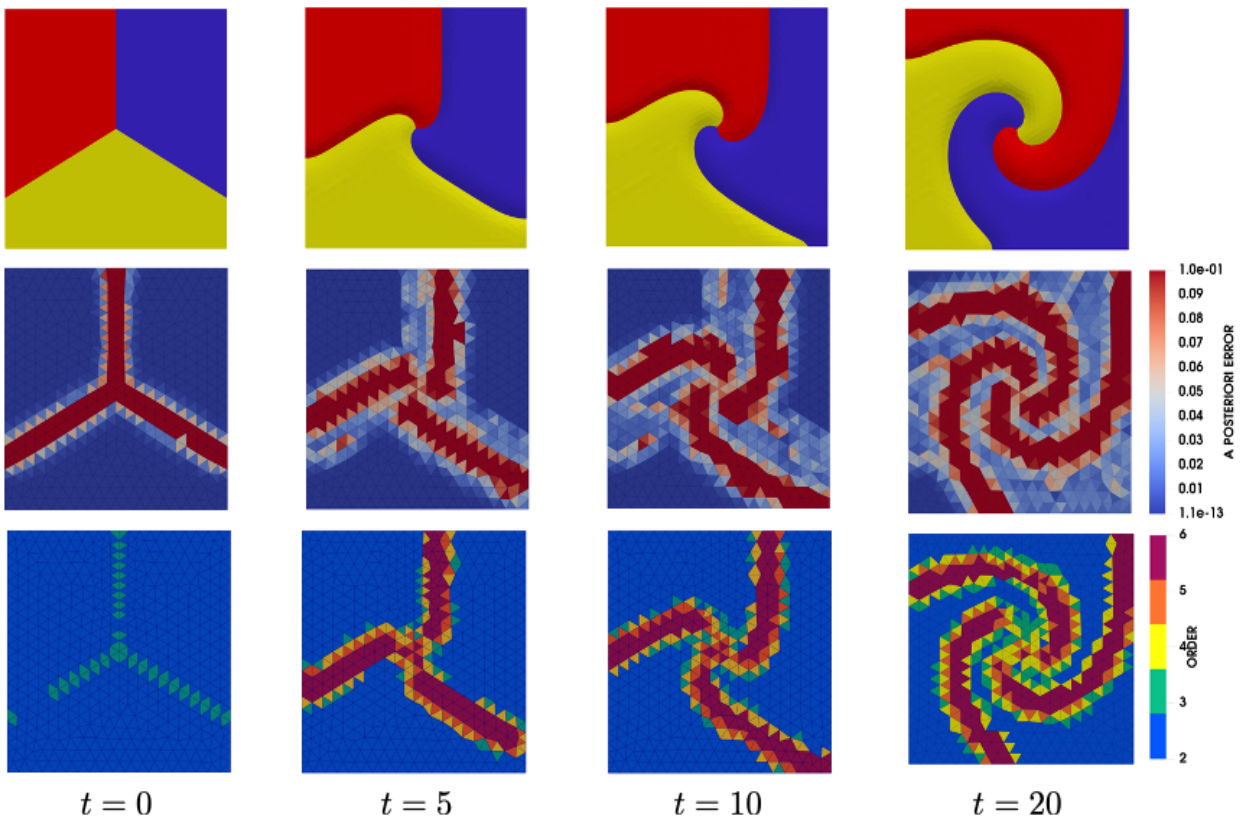


Figure 16: Development of spiral pattern as a result of cyclic interactions of three species (Equation (42), Table 2) at various stages. Region with blue depicts  $m_1$ , red  $m_2$ , and green  $m_3$ .



Table 3: List of parameters for spiral wave re-entry problem

$d$	$\alpha$	$\gamma$	$b$	$c$	$\mu$	$\mu_2$
[mm <sup>2</sup> ]	[-]	[-]	[-]	[-]	[-]	[-]
0.01	0.01	0.01	1	2	7	7

$r$  is a single internal variable representing the density of ionic channels, and  $I_{\Omega'}$  is the external stimulus. The time  $t$  [ms] is non-dimensionalised as

$$t = 12.9\tau \text{ ms.}$$

One of the simplest models capable of reproducing the spiral wave re-entry, the Aliev-Panfilov model [12], is adopted for the reaction term:

$$f(m, r) = cm[m - \alpha][1 - m] - rm. \quad (44)$$

Equation (44) is supplemented by an ordinary differential equation for the recovery (internal state) variables  $r$ :

$$\frac{d}{d\tau}r = \left[ \gamma + \frac{\mu_1 r}{\mu_2 + m} \right] [-r - cm[m - b - 1]], \quad (45)$$

where the parameters appearing in equations (44) and (45) are given in Table 3. We assume the conductivity to be isotropic, i.e.,  $\mathbf{D} = d\mathbf{I}$ . The simulation is carried out using the IMEX mixed formulation with order  $k = 1$  (recall that  $k$  is the polynomial order used for the approximation of  $m$  and  $k + 1$  is the order used for the flux). The p-adaptivity strategy with parameters  $\theta_{\max} = 0.7$  and  $\theta_{\min} = 0.03$  starts with uniformly order 2 and increases locally to order 6.

A horizontal planar wave is initiated by setting the action potential to  $E = -40$  mV on the region between  $y = 0$  and  $y = 3$ . The wave form continues to propagate upwards as seen from the snapshot at  $t = 160$  ms.

Before the depolarising tail disappears, an external stimulus  $I_{\Omega'}$  is applied to the strip of region, defined by  $\Omega' = \{(x, y) : 50 < x < 100, 67 < y < 70\}$ , in order to initiate the spiral wave re-entry. The stimulus has magnitude 40 and is applied at  $t = 565$  ms for a duration of 10 ms. This results in the development of the wavebreak (shown in Fig. 17 at  $t = 7722$  ms). The wavebreak then evolves into a stable rotating vortex, as shown in the snapshots at  $t = 924$  ms, and continues afterwards.

The computational aspects of this problem have been considered by several researchers in the electrophysiology and electromechanics community. One notable work is by Göktepe and Kuhl [50] in which they used the standard finite element approach with an implicit time integration scheme on a structured quad mesh. The proposed p-adaptive, IMEX mixed, as compared to their work, method is seen to capture the spiral wave re-entry dynamics more efficiently.

## 8. Conclusion

A family of p-adaptive implicit-explicit, mixed finite element formulations has been proposed for a general class of reaction-diffusion based problems. In contrast to single-field, standard finite element formulations, this class of methods provides accurate approximations of a wider class of solutions, including those with less regularity. A standard formulation was shown to converge poorly, if at all, for such problems. The IMEX approach has been shown to be efficient and eliminates the dependence of algorithmic stability on the size of the spatial mesh size by handling the non-local diffusion part implicitly. This advantageous feature allows for mesh refinement, for example in an adaptive strategy, without the need for changing the time step size,  $\Delta t$ . The explicit treatment of the local reaction term makes the implementation generic and modular for various classes of reaction kinetics as demonstrated by the wide range of problems that have been analysed in this paper. The finite element spaces are built using a hierarchical construction which, in addition to offering optimal conditioning of the resulting linear system, makes the use of the  $p$ -adaptivity strategy a natural choice [39]. The mixed formulation introduces additional DoFs. However, the computational complexity due to this increase in DoFs can be handled efficiently using static condensation as the mass concentration field (which is in  $L^2$ ) can be inverted locally since the local contributions are decoupled from one another. Moreover, this local inversion can also be used in block iterative schemes that involves computation of the

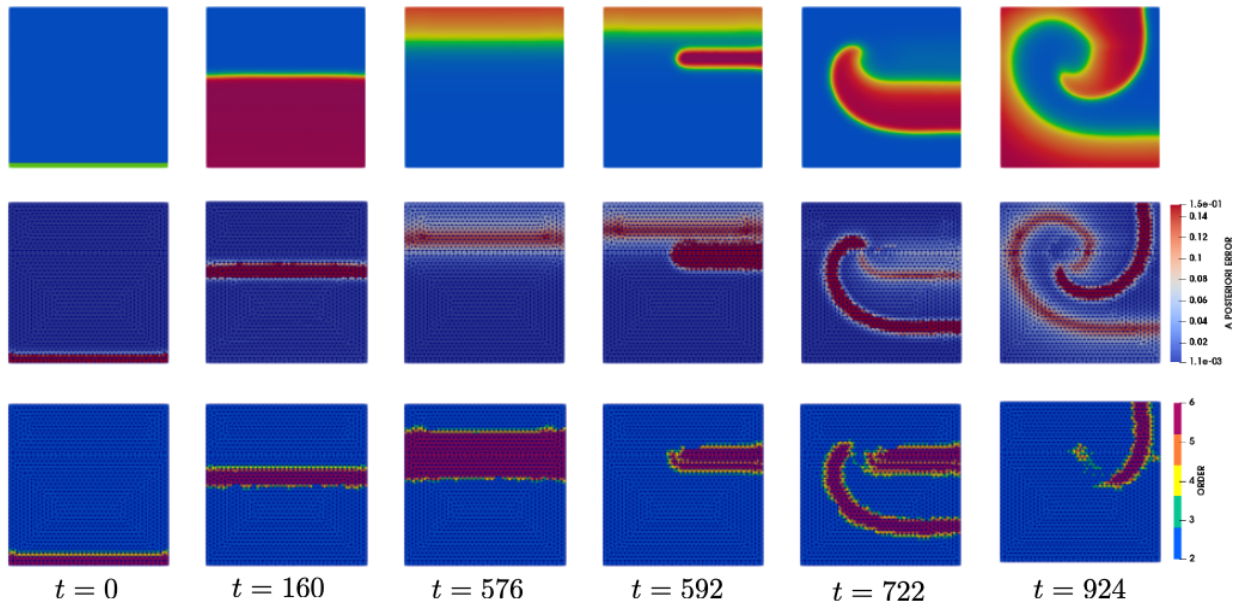


Figure 17: Evolution of a planar wave into a rotating spiral wave re-entry as a result of external stimulation  $I_{\Omega'} = 40$  applied on the red shaded region (top left) during the time interval  $t = 570$  ms to  $t = 580$  ms. The planar wave is initiated with an initial excitation of  $E(t = 0) = -40$  mV on the region shaded in blue.

Schur complement as an intermediate step. The Schur complement can then be computed exactly, resulting in a sparse global structure, rather than reverting to the common practice of approximating it.

A distinguishing feature of the mixed formulation is that it leads to straightforward derivation and implementation of residual based a posteriori error estimations without the need for computationally demanding postprocessing effort as it is usually the case in literature, see, for example, [53–55]. This feature together with the hierarchical approximation of the mixed finite element method is exploited in formulating the p-adaptive strategy. It has been demonstrated by a range of examples that the p-adaptive algorithm performs very well in efficiently resolving fine features.

The performance of the proposed formulation is demonstrated by a number of challenging examples. The advantages of the proposed method over the standard techniques are showcased by the following two examples: a problem that has singularities (see Section 7.1); and one that supports travelling wave solutions (see Section 7.2). The capability of this general p-adaptive framework is demonstrated by applying it to problems arising from different applications such as electrophysiology [12, 50], and spatial pattern formation in theoretical ecology [6, 51, 52].

Through a generalisation straightforwardly the proposed mixed method can be coupled to the mechanical deformation field for applications in cardiac electromechanics and chemo-mechanics. Due to the explicit treatment of the reaction term, the approach can be easily linked with, for example, electrophysiology models in the CellML repository [55]. Similarly, due to this explicit treatment of the reaction term, our computational approach can be easily used to drive the form of reaction kinetics models from experimental data following the approach proposed in [56].

## Acknowledgements

The authors gratefully acknowledge the support provided by the EPSRC Strategic Support Package: Engineering of Active Materials by Multiscale/Multiphysics Computational Mechanics - EP/R008531/1.

## References

## References

- [1] M. Chaplain, M. Ganesh, I. Graham, Spatio-temporal pattern formation on spherical surfaces: Numerical simulation and application to solid tumour growth, *Journal of Mathematical Biology* 42 (5) (2001) 387–423.
- [2] K. Garikipati, Perspectives on the mathematics of biological patterning and morphogenesis, *Journal of the Mechanics and Physics of Solids* 99 (2017) 192 – 210.
- [3] P. K. Tapaswi, A. K. Saha, Pattern formation and morphogenesis: A reaction-diffusion model, *Bulletin of Mathematical Biology* 48 (2) (1986) 213 – 228.
- [4] S. F. Gilbert, *Mathematical Modeling of Development*, developmental biology, 6th edition Edition, Sinauer Associates, 2000.
- [5] D. Ambrosi, G. A. Ateshian, E. M. Arruda, S. C. Cowin, J. Dumais, A. Goriely, G. A. Holzapfel, J. D. Humphrey, R. Kemkemer, E. Kuhl, J. E. Olberding, L. A. Taber, K. Garikipati, Perspectives on biological growth and remodeling, *Journal of the Mechanics and Physics of Solids* 59 (4) (2011) 863 – 883.
- [6] Y. Morishita, Y. Iwasa, Growth based morphogenesis of vertebrate limb bud, *Bulletin of Mathematical Biology* 70 (7) (2008) 1957–1978.
- [7] M. Tewary, J. Ostblom, L. Prochazka, T. Zulueta-Coarasa, N. Shakiba, R. Fernandez-Gonzalez, P. W. Zandstra, A stepwise model of reaction-diffusion and positional information governs self-organized human peri-gastrulation-like patterning, *Development* 144 (23) (2017) 4298–4312.
- [8] A. M. Sebastian, M. Adrian, A two-scale reaction–diffusion system with micro-cell reaction concentrated on a free boundary, *Comptes Rendus Mécanique* 336 (6) (2008) 481–486.
- [9] M. D. Ryser, S. V. Komarova, N. Nigam, The cellular dynamics of bone remodeling: A mathematical model, *SIAM Journal on Applied Mathematics* 70 (6) (2010) 1899–1921.
- [10] J. S. Matthew, A. L. Kerry, F. N. Donald, Chemotactic and diffusive migration on a nonuniformly growing domain: numerical algorithm development and applications, *Journal of Computational and Applied Mathematics* 192 (2) (2006) 282 – 300.
- [11] R. C. P. Kerckhoffs, S. N. Healy, T. P. Usyk, A. D. McCulloch, Computational methods for cardiac electromechanics, *Proceedings of the IEEE* 94 (4) (2006) 769–783.
- [12] R. Aliev, A. Panfilov, A simple two-variable model of cardiac excitation, *Chaos Solitons and Fractals* 7 (3) (1996) 293–301.
- [13] Y. Zhang, X.-Q. Zhao, A reaction-diffusion lyme disease model with seasonality, *SIAM Journal on Applied Mathematics* 73 (6) (2013) 2077–2099.
- [14] W. Wang, X.-Q. Zhao, A nonlocal and time-delayed reaction-diffusion model of dengue transmission, *SIAM Journal on Applied Mathematics* 71 (1) (2011) 147–168.
- [15] R. E. Wilson, V. Capasso, Analysis of a reaction-diffusion system modeling man–environment–man epidemics, *SIAM Journal on Applied Mathematics* 57 (2) (1997) 327–346.
- [16] M. Hemami, K. Parand, J. A. Rad, Numerical simulation of reaction-diffusion neural dynamics models and their synchronization/desynchronization: Application to epileptic seizures, *Computers and Mathematics with Applications* 78 (11) (2019) 3644–3677.
- [17] D. Olmos, B. D. Shizgal, Pseudospectral method of solution of the fitzhugh–nagumo equation, *Mathematics and Computers in Simulation* 79 (7) (2009) 2258–2278.
- [18] J. Ramos, A review of some numerical methods for reaction-diffusion equations, *Mathematics and Computers in Simulation* 25 (6) (1983) 538–548.
- [19] D. Barkley, A model for fast computer simulation of waves in excitable media, *Physica D: Nonlinear Phenomena* 49 (1) (1991) 61–70.
- [20] R. Ruiz-Baier, Primal-mixed formulations for reaction-diffusion systems on deforming domains, *Journal of Computational Physics* 299 (2015) 320–338.
- [21] J. Lang, Adaptive fem for reaction-diffusion equations, *Applied Numerical Mathematics* 26 (1) (1998) 105–116.
- [22] N. Tuncer, A. Madzvamuse, A. Meir, Projected finite elements for reaction–diffusion systems on stationary closed surfaces, *Applied Numerical Mathematics* 96 (2015) 45–71.
- [23] G. MacDonald, J. A. Mackenzie, M. Nolan, R. H. Insall, A computational method for the coupled solution of reaction–diffusion equations on evolving domains and manifolds: Application to a model of cell migration and chemotaxis, *Journal of Computational Physics* 309 (2016) 207–226.
- [24] C. Landsberg, A. Voigt, A multigrid finite element method for reaction-diffusion systems on surfaces, *Computing and Visualization in Science* 13 (2010) 177–185.
- [25] W. D. Mergia, K. C. Patidar, High-order semi-implicit linear multistep lg scheme for a three species competition-diffusion system in two-dimensional spatial domain arising in ecology, *Communications in Nonlinear Science and Numerical Simulation* 84 (2020) 1–16.
- [26] D. Boffi, F. Brezzi, M. Fortin, *Mixed finite element methods and applications*, Springer Series in Computational Mathematics, Springer, Berlin, 2013.
- [27] L. P. Franca, T. J. Hughes, Two classes of mixed finite element methods, *Computer Methods in Applied Mechanics and Engineering* 69 (1) (1988) 89–129.
- [28] D. N. Arnold, Mixed finite element methods for elliptic problems, *Computer Methods in Applied Mechanics and Engineering* 82 (1) (1990) 281–300.
- [29] H. Fu, H. Guo, J. Hou, J. Zhao, A stabilized mixed finite element method for steady and unsteady reaction–diffusion equations, *Computer Methods in Applied Mechanics and Engineering* 304 (2016) 102 – 117.
- [30] S. Liu, Y. Chen, A new two-grid method for expanded mixed finite element solution of nonlinear reaction diffusion equations, *Advances in Applied Mathematics and Mechanics* 9 (3) (2017) 757–774.
- [31] S. J. Ruuth, Implicit-explicit methods for reaction-diffusion problems in pattern formation, *Journal of Mathematical Biology* 34 (2) (1995) 148–176.

- [32] U. M. Ascher, S. J. Ruuth, B. T. R. Wetton, Implicit-explicit methods for time-dependent partial differential equations, *SIAM Journal on Numerical Analysis* 32 (3) (1995) 797–823.
- [33] H. Zhang, A. Sandu, Application of implicit-explicit general linear methods to reaction-diffusion problems, *AIP Conference Proceedings* 1648 (1) (2015) 150017.
- [34] I. Faragó, F. Izsák, T. Szabó, A. Kriston, An imex scheme for reaction-diffusion equations: application for a pem fuel cell model, *Open Mathematics* 11 (4) (2013) 746–759.
- [35] O. Lakkis, A. Madzvamuse, C. Venkataraman, Implicit-explicit timestepping with finite element approximation of reaction-diffusion systems on evolving domains, *SIAM Journal on Numerical Analysis* 51 (4) (2013) 2309–2330.
- [36] J. Lin, S. Reutskiy, A cubic b-spline semi-analytical algorithm for simulation of 3d steady-state convection-diffusion-reaction problems, *Applied Mathematics and Computation* 371 (2020) 124944.
- [37] C. A. Kennedy, M. H. Carpenter, Additive runge–kutta schemes for convection–diffusion–reaction equations, *Applied Numerical Mathematics* 44 (1–2) (2003) 139–181.
- [38] C. A. Kennedy, M. H. Carpenter, Higher-order additive runge–kutta schemes for ordinary differential equations, *Applied Numerical Mathematics* 136 (2019) 183–205.
- [39] M. Ainsworth, J. Coyle, Hierarchic finite element bases on unstructured tetrahedral meshes, *International Journal for Numerical Methods in Engineering* 58 (14) (2003) 2103–2130.
- [40] B. Guo, I. Babuska, S. N. Atluri, The h-p version of the finite element method. i: The basic approximation results, *Computational Mechanics* 1 (1986) 203–220.
- [41] I. Babuska, W. Gui, The h, p and h-p versions of the finite element method in 1 dimension. part iii. the adaptive h-p version, *Numerische Mathematik* 49 (1986) 659–684.
- [42] F. Fuentes, B. Keith, L. Demkowicz, S. Nagaraj, Orientation embedded high order shape functions for the exact sequence elements of all shapes, *Computers & Mathematics with Applications* 70 (4) (2015) 353–458.
- [43] W. Dörfler, V. Heuveline, Convergence of an adaptive hp finite element strategy in one space dimension, *Applied Numerical Mathematics* 57 (10) (2007) 1108–1124.
- [44] Ł. Kaczmarczyk, Z. Ullah, K. Lewandowski, X. Meng, X.-Y. Zhou, I. Athanasiadis, H. Nguyen, C.-A. Chalons-Mouriesse, E. Richardson, E. Miur, A. Shvarts, M. Wakeni, C. Pearce, MoFEM: an open source, parallel finite element library, *The Journal of Open Source Software*.
- [45] T. J. Tautges, C. Ernst, C. Stimpson, R. J. Meyers, K. Merkle, Moab : a mesh-oriented database (2004).  
URL <https://www.osti.gov/biblio/970174>
- [46] T. Tautges, Moab-sd: integrated structured and unstructured mesh representation, *Engineering with Computers* 20 (2004) 286–293.
- [47] S. Balay, W. D. Gropp, L. C. McInnes, B. F. Smith, Efficient management of parallelism in object oriented numerical software libraries, in: E. Arge, A. M. Bruaset, H. P. Langtangen (Eds.), *Modern Software Tools in Scientific Computing*, Birkhäuser Press, 1997, pp. 163–202.
- [48] S. Balay, S. Abhyankar, M. F. Adams, J. Brown, P. Brune, K. Buschelman, L. Dalcin, A. Dener, V. Eijkhout, W. D. Gropp, D. Karpeyev, D. Kaushik, M. G. Knepley, D. A. May, L. C. McInnes, R. T. Mills, T. Munson, K. Rupp, P. Sanan, B. F. Smith, S. Zampini, H. Zhang, H. Zhang, PETSc Web page (2019).  
URL <https://www.mcs.anl.gov/petsc>
- [49] S. Abhyankar, J. Brown, E. M. Constantinescu, D. Ghosh, B. F. Smith, H. Zhang, *Petsc/ts: A modern scalable ode/dae solver library*, arXiv preprint arXiv:1806.01437.
- [50] S. Göktepe, E. Kuhl, Computational modeling of cardiac electrophysiology: A novel finite element approach, *International Journal for Numerical Methods in Engineering* 79 (2) (2009) 156–178.
- [51] M. Mimura, M. Tohma, Dynamic coexistence in a three-species competition–diffusion system, *Ecological Complexity* 21 (2015) 215–232.
- [52] M. Mimura, Y. Kan-on, Dynamic coexistence in a three-species competition–diffusion system, *Predation-Mediated Coexistence and Segregation Structures* 18 (1986) 129–155.
- [53] M. Ainsworth, A posteriori error estimation for lowest order raviart–thomas mixed finite elements, *SIAM Journal on Scientific Computing* 30 (1) (2008) 189–204.
- [54] D. Braess, R. Verfürth, A posteriori error estimators for the raviart-thomas element, *SIAM Journal on Numerical Analysis* 33 (6) (1996) 2431–2444.
- [55] C. M. Lloyd, T. Yu, Cellml model repository, in: W. Dubitzky, O. Wolkenhauer, K.-H. Cho, H. Yokota (Eds.), *Encyclopedia of Systems Biology*, Springer New York, New York, NY, 2013, pp. 376–378.
- [56] S. L. Brunton, J. L. Proctor, J. N. Kutz, Discovering governing equations from data by sparse identification of nonlinear dynamical systems, *Proceedings of the National Academy of Sciences* 113 (15) (2016) 3932–3937.